Deformation behavior and inferred seismic properties of tonalitic migmatites at the time of pre-melting, partial melting and post-solidification

Yongjiang Liu[1], Yilun Shao[2], and Sandra Piazolo[3]

[1]Key Lab of Submarine Geoscience and Prospecting Techniques, MOE, College of Marine Geosciences, Ocean University of China
[2]College of Earth Sciences, Jilin University,
[3]School of Earth and Environment, University of Leeds

November 24, 2022

Abstract

As seismic data from the lower crust becomes more readily available, it is import ant to link seismic properties to the ongoing processes within lower crustal evolution. It includes high temperature, pre- and post-migmatisation solid state deformation as well as melt-present deformation condition. We selected two tonalitic migmatites with variable former melt content (one metatexite and one diatexite) from the lower crustal Daqingshan area, northern North China Craton (NCC) to assess the link between seismic properties and rock structure and rheology. Field observation along with microstructural features suggest that the character of hornblende and plagioclase within the residuum of the metatexite can be used to derive information regarding the pre-migmatisation deformation. Residuum's plagioclase CPO (crystallographic preferred orientation) is consistent with high temperature dislocation creep as the main deformation mechanism; similarly, hornblende shows a strong CPO related to dislocation creep. During syn-melt (melt present) conditions, phenocrysts of plagioclase in the metatexite's neosome and K-feldspar and peritectic hornblende in the diatexite's neosome are present. The rheology of the rock was dominated by melt; hence is inferred to follow Newtonian flow. After melt crystallization deformation is minor but again dominated by dislocation creep. For seismic properties (seismic velocity, anisotropy, Vp/Vs ratio, etc.), in pre- and post-melt conditions, migmatites have normal values. While in syn-melt condition, seismic velocities have a greater decrease, Vp/Vs ratios have a great increase, seismic anisotropies are unusually high.

Deformation behavior and inferred seismic properties of tonalitic migmatites at the time of pre-melting, partial melting and post-solidification

Yilun Shao[1, 2], Sandra Piazolo[3, 4], Yongjiang Liu[5, 6*], Amicia L Lee[7], Wei Jin[1], Weimin Li[1], Chenyue Liang[1], Quanbo Wen[1]

[1] *College of Earth Sciences, Jilin University, Jianshe Str. 2199, 130061 Changchun, Jilin, China.*

[2] *Department of Geology, University of Otago, PO Box 56, Dunedin 9054, New Zealand.*

[3] *School of Earth and Environment, University of Leeds, Leeds, LS2 9JT, UK.*

[4] *Australian Research Council of Excellence for Core to Crust Fluid Systems/GEMOC, Department of Earth and Planetary Sciences, Macquarie University, NSW, 2109, Australia.*

[5] *Key Lab of Submarine Geoscience and Prospecting Techniques, MOE, Institute for Advanced Ocean Study, College of Marine Geosciences, Ocean University of China, Qingdao 266100, China.*

[6] *Laboratory for Marine Mineral Resources, Qingdao National Laboratory for Marine Science and Technology, Qingdao 266237, China.*

[7] *Department of Geosciences, University of Tromsø, Tromsø, 9037, Norway.*

Email address (* represents corresponding author):

Yilun Shao: shayi182@student.otago.ac.nz Sandra Piazolo: S.Piazolo@leeds.ac.uk Yongjiang Liu*: liuyongjiang@ouc.edu.cn Amicia L Lee: amicia.lee@uit.no Wei Jin: jinwei@jlu.edu.cn Weimin Li: weiminli@jlu.edu.cn Chenyue Liang: chenyueliang@jlu.edu.cn Quanbo Wen:

58165315@qq.com

Key points:

Tonalitic migmatites show distinct deformation signatures and seismic properties during pre-, syn-, and post-migmatisation.

Power-law creep dominates solid phases' deformation, near-Newtonian flow is typical for deformation in rocks with high melt content.

Migmatites have low Vs and extreme high seismic anisotropies in syn-melt condition.

Abstract:

As seismic data from the lower crust becomes more readily available, it is important to link seismic properties to the ongoing processes within lower crustal evolution. It includes high temperature, pre- and post-migmatisation solid state deformation as well as melt-present deformation condition. We selected two tonalitic migmatites with variable former melt content (one metatexite and one diatexite) from the lower crustal Daqingshan area, northern North China Craton (NCC) to assess the link between seismic properties and rock structure and rheology. Field observation along with microstructural features suggest that the character of hornblende and plagioclase within the residuum of the metatexite can be used to derive information regarding the pre-migmatisation deformation. Residuum's plagioclase CPO (crystallographic preferred orientation) is consistent with high temperature dislocation creep as the main deformation mechanism; similarly, hornblende shows a strong CPO related to dislocation creep. During syn-melt (melt present) conditions, phenocrysts of plagioclase in the metatexite's neosome and

K-feldspar and peritectic hornblende in the diatexite’s neosome are present. The rheology of the rock was dominated by melt; hence is inferred to follow Newtonian flow. After melt crystallization deformation is minor but again dominated by dislocation creep. For seismic properties (seismic velocity, anisotropy, Vp/Vs ratio, etc.), in pre- and post-melt conditions, migmatites have normal values. While in syn-melt condition, seismic velocities have a greater decrease, Vp/Vs ratios have a great increase, seismic anisotropies are unusually high.

Keywords: migmatite; EBSD; rheology, seismic properties, syn-migmatisation, post-migmatisation

1. Introduction

The rheological behavior of the lower crust is still under continuous debate (e.g. jelly sandwich, crème brûlée and banana split; Burov & Diament, 1995; Jackson, 2002; Bürgmann & Dresen, 2008), and the geophysical information is of pivotal importance to our understanding of lithospheric flow behavior governing the lower crust of orogenies (Rudnick & Fountain, 1995; Bürgmann & Dresen, 2008; Almqvist & Mainprice, 2017). Migmatites are an important rock type in the lower crust, hence it is important to investigate the related deformation process to infer the rheological evolution of the lower crust (Vanderhaeghe & Teyssier, 2001; Hasalová et al., 2008). Understanding deformation mechanisms and geophysical implications of the two main stages of migmatization, partial melting and rock solidification, are essential if one is to recover lower crust evolution and its rheology (Dell’ Angelo et al., 1988; Gómez Barreiro et al., 2007; Almqvist et al., 2015; Miranda & Klepeis, 2016; Almqvist & Mainprice, 2017). Generally, the domain that is slightly influenced by partial melting preserves predominantly the rock's geological history before melting (referred to as residuum; Guernina & Sawyer, 2003; Sawyer, 2008). In contrast, the neosome (or referred to as leucosome, melanosome, etc.) represents the former melt-dominated area (Kriegsman & Hensen, 1998; Kriegsman, 2001; Sawyer & Brown, 2008). In addition, granitic rocks (e.g. granite, diorite, tonalite) in partial melting condition would generate K-feldspar and quartz (Tuttle and Bowen, 1958; Barker and Arth, 1976; Barker et al., 1981).

During partial melting in the lower crust, the deformation behavior of a rock is mainly determined by the melt fraction and its distribution. At low melt fractions (2-4%), dislocation creep (e.g. grain boundary migration, short for GBM) may be active (Walte et al., 2005; Závada et al., 2007). With higher melt fractions (e.g. ~7%), the grain boundary sliding (GBS) is activated, and is usually diffusion creep dominant (Cooper & Kohlstedt, 1984; Hasalová et al., 2008; Závada et al., 2018). If the melt fraction is larger than 8%, granular flow plays a main role (Paterson, 2001; Walte et al., 2005). Microscopic observation shows that a rock melt may exist as intracrystalline inclusions trapped in grains (e.g. triple junction; Copper and Kohlstedt 1984; Sawyer, 2001; Walte et al., 2005; Závada et al., 2007) or as a connected melt network along grain boundaries (Dell' Angelo et al., 1988; Stuart et al., 2017, 2018). At high melt fraction (e.g. >10%) melt becomes segregated into bands, the rheological behavior of the bulk rock will be dominated by that of the melt bands (e.g. Newtonian; Burg & Vigneresse, 2002; Rosenberg & Handy, 2005; Champallier et al., 2008).

It is clear that partial melting strongly affects the seismic properties of rocks and also affects P- and S-wave velocities differently resulting in changing Vp/Vs-ratios. (Hammond & Humphreys, 2000; Franěk et al., 2006, 2011; Lee et al., 2017). Miranda & Klepeis (2016) indicate that dislocation creep is the dominant deformation mechanism in melt-frozen rocks (or crystalized melt). However, microstructural analysis of migmatites show that once a migmatite is crystallized, deformation characteristics might not so strong and bulk strain in such rock is minor (Prakash et al. 2018).

The seismic properties of lower crustal rocks are influenced by not only mineral modal content (Rudnick & Fountain, 1995; Lloyd et al., 2011), but also by metamorphic banding (Cyprych et al. 2017) and constituent minerals' (e.g. hornblende and biotite) CPO (crystallographic preferred orientation) (Tatham et al. 2008; Lloyd et al., 2011). Melt production will decrease both P-wave (Vp) and S-wave (Vs), Vs would be more influenced and lead to high Vp/Vs (Schilling & Partzsch, 2001; Almqvist et al., 2015; Ferri et al., 2016). Seismic low-velocity zones are inferred to represent zones of partial molten lower crust (Caldwell et al., 2009; Xie et al., 2013; Lee et al., 2017). During partial melting period, seismic anisotropy might be increased by layered melt or grains' crystallographic orientation (Holtzman & Kendall et al., 2010; Almqvist et al., 2015) or decreased by breakdown of highly anisotropic minerals (e.g. micas) or tube distribution of melt (Hacker et al., 2014; Ferri et al., 2016). In addition, studies have shown that the Vp/Vs ratio may be useful to infer the partial melting degree (Nábelek et al., 2009; Ferri et al., 2016, Lee et al., 2017). Hacker et al. (2014) established a model to predict seismic velocities in current partially molten rocks in Central Tibet (Qiangtang block), suggesting that low shear wave velocity (~3.3 km/s) might due to melt injection from the deeper crust. Furthermore, a Vp/Vs of 2 has been suggested to indicate partial melting at intermediate depth (Julià et al., 2005). Studies of seismic properties of post-migmatisation lower crustal rocks are rare. Hacker et al. (2014) showed in their model that crystallized melt would be expected to decrease Vs, with seismic properties mimicking that of partially molten rocks.

Over the last 20 years, electron backscatter diffraction (EBSD) analysis (Venables & Harland, 1973; Prior et al., 1999), which enables determination of the CPO of the main minerals in a rock, has been applied to calculate seismic properties (Mainprice, 1990; Mainprice et al., 2011). Therefore, it is possible to infer the geophysical properties from a rock specimen (Tatham et al. 2008; Lloyd et al., 2011; Ferré et al., 2014; Lamarque et al., 2016; Almqvist & Mainprice, 2017; Cyprych et al. 2017). So far, research computing seismic responses (e.g. velocity, anisotropy, Vp/Vs ratio, etc.) from natural examples has utilized data from a whole rock (Rudnick & Fountain, 1995; Hacker et al., 2014). In the case of a migmatites, however, different domains which each has its own properties need to be taken into account to decipher the different seismic signals at the different stages of the rock's history (i.e. protolith prior to melting, partial melting, migmatization, melt frozen, etc.). Hence, assessing the properties of the different parts of the migmatite would allow for an improvement of our ability to link seismic characteristics to partial melting and/or melt frozen status. At the same time, since different degrees of melting occur in the lower crust (Vanderhaeghe, 2001; Sawyer, 2014), exploring the effect of such different melt fractions within the same rock type is important (Lee et al. 2017). To improve our ability to assess seismic data in the light of absence, presence or former presence of melt, it is important to assess the evolution of seismic properties of a migmatitic unit taking its properties pre-, syn- and post-melting into account. Consequently, in this study we aim to investigate the behavior of a migmatites before, during and after melting. In particular we focus on: (1) the deformation characteristics and deformation evolution in different migmatite domains of two rock samples with differing former melt fraction; (2) their rheological behavior through their geological evolution; and (3) their seismic signature during partial melting and post-melting, in the melt-frozen status.

The studied samples stem from the Daqingshan area of the northern North China Craton (NCC), China (Figure 1), where a series of anatectic lower crustal rocks with clear migmatitic signatures is preserved without later overprint (Jin et al., 1991, 1992; Yang et al., 2008; Cai, Liu, Liu, Liu, et al., 2013; Cai, Liu, Liu, Shi & Liu, 2013; Cai et al., 2014; Ma et al., 2015). The migmatites are derived from largely the same rock type that exhibit different melt percentages during anatexis (Li et al., 1995; Yang et al., 2008). In this paper, based on the detailed petrographic studies, we use EBSD analysis to explore migmatites' microstructures and orientation characteristics. This data is be used to derive deformation mechanism in pre-melting (pre-melt), syn-anatexis (syn-melt) and post anataxis (post-melt) conditions, as well as to calculate expected seismic properties.

2. General geological setting

The study area Daqingshan was chosen as it exhibits migmatitic rocks of different types without significant retrograde overprinting, so that it is rendered as an ideal place to study the nature of lower crustal migmatites. The study area lies in the middle "Khondalite Belt" between Yinshan Block and Ordos Block, which constitute the main part of the Western Block of northern North China Craton (NCC; Zhao, et al., 2005, 2012; Santosh et al., 2007, 2009; Guo et al., 2012; Zhao & Guo, 2012; see Figure 1a inset). The current model for the evolution of NCC is that Yinshan and Ordos Block amalgamated along the E-W trending Khondalite Belt during a Precambrian event (1.95-1.92 Ga) forming the Western Block, around 1.85 Ga the Trans-North China Orogen (TNCO) was formed by collision with the Eastern Block (Zhao, et al., 2002, 2005, 2012; Zhao, 2007, see Figure 1a's inset). Associated with the latter collision is the high grade Khondalite Belt which is dominated by metasediments with subvertical foliations (Figure 1b) and several E-W trending steep ductile shear zones (Yang et al., 2008; Gong et al., 2014).

The Daqingshan area is dominated by a series of Precambrian metamorphic rocks from Late Neoarchean to Late Paleoproterozoic. It mainly includes metamorphosed TTG (Trondhjemite-Tonalite-Granodiorite, around 2.5 Ga), mafic granulite (metamorphic gabbro, Sanggan Group, Late Neoarchean), banded gneiss (Lower Wulashan Group, Late Archean-Early Paleoproterozoic), metasediments (Upper Wulashan Group or Khondalite series, Late Paleoproterozoic), Daqingshan supracrustal rocks (2.50-2.45 Ga)), and granitic gneiss (Late Paleoproterozoic) (Jin et al., 1991, 1992; Xu et al., 2007, 2015; Yang et al., 2008; Ma, Wan, Santosh, et al., 2012; Ma, Wan, Xu, et al., 2012; Wan et al., 2009, 2013; Dong et al., 2014; see Figure 1). Cai, Liu, Liu, Liu, et al. (2013), Cai, Liu, Liu, Shi & Liu (2013) and Cai et al. (2014) used metapelite assemblages to determine peak metamorphic PT conditions (granulite facies) in the area around Hujigou (close to the studied metatexite sample 16BT28-11; Figure 1) to be 647-870 ℃, 5.6-8.6 kbar and 800-920 ℃, 8.1-12.5 kbar near Xuehaigou (close to the studied diatexitic sample 16BT14-3; Figure 1), which is close to granulite facies. These pressure and temperature conditions are supported by the general observation: from north to south the metamorphic grade is increasing, shown as successively higher amount of felsic material, intercalated with a more mafic gneiss (Figures 1 and 2). This is interpreted to represent a N-S increase in the degree of local melting and reaching a peak in the southern research area (near Xuehaigou), where flow features are common and thick bands of felsic material are ubiquitous in outcrop (Figure 2; Ma, Wan, Xu, et al., 2012; Xu et al., 2015).

3. Definition of terms and methods

3.1. Definition of terms

The term migmatite defines the rock has at least two different petrographical parts, which is influenced by presence of melt in medium-high grade metamorphic environments (Olsen, 1977; Kriegsman, 2001; Maxeiner et al., 2017). We follow Sawyer & Brown (2008) and define the parts which experienced partial melting as "residuum" domains. In this case study, residuum domains are formed by unmelted minerals and minor crystallized melt. For the parts with solid phase and abundant crystallized melt, they are dominated by either felsic minerals (or defined as "leucosome") or dark minerals (or defined as "melanosome") (Figure 3; Johannes and Gupata, 1982; Kriegsman & Hensen, 1998; Kriegsman, 2001), which we termed as "neosome" (Olsen, 1977; Sawyer et al., 2011) for simplifying the descriptions of migmatite evolution. Based on the definition above, we assume that in single migmatite sample, residuum domain has stronger deformation characteristics than neosome domain, and in neosome domain, the solid phase has stronger deformation characteristics than crystalized melt. In this contribution the melt fraction is used to divide sampled migmatites into metatexite (<26 melt%) and diatexite (>26 melt%) (Sawyer & Brown, 2008).

3.2. Sample selection and preparation

To explore the deformation behavior and seismic properties of typical lower crustal migmatic rocks, we selected two representative samples of broadly tonalitic composition with a general assemblage of hornblende, feldspar and minor quartz (Figure 1 and Table 1). The two samples are chosen as they represent migmatites with different amounts of leucocratic material, which might be the former melt (Figures 1 and 2). Polished thin sections were prepared from blocks cut perpendicular to the foliation (XY section) and parallel to lineation (X axis).

Sample 16BT28-11 represents a metatexite, which shows clearly separated residuum and neosome (leucosome) domains (Figure 3a and Table 1). In hand specimen the felsic injections make up 15-20% of the rock (Figure 3a). Residuum is dominated by hornblende and plagioclase, where hornblende grains are aligned subparallel to the main foliation. Neosome is dominated by felsic minerals (mainly K-feldspar with subordinate plagioclase) and the domain is vein-shaped and subparallel to the foliation and injects the residuum (Figure 3a and Table 1).

Sample 16BT14-3 represents a diatexite which is neosome dominated. The residuum plagioclase grains are associated with lineation-parallel biotite (Figure 3b). K-feldspar takes up 15% of the residuum, higher in abundance than in the metatexite's residuum. The neosome forms larger areas in thin section (Figure 3b), and K-feldspar makes up 13.5% (Table 1). Hornblende is the main mineral of diatexite's neosome (37.8%), the grains are commonly slightly inclined to lineation (Figure 3b and Table 1).

General mineral information such as grain shape, mineral assemblages and optical characteristics were collected using a petrographic microscope. Before Electron Backscatter Diffraction (EBSD) and EDS (energy-dispersive X-ray spectroscopy) analysis the sections were polished using mechano-chemical colloidal silica and coated with carbon (about 3 nm). A thicker coat was applied for the separate microchemical maps attained by electron microprobe.

3.3. Quantitative crystallographic orientation analysis - EBSD

Quantitative crystallographic orientation data was obtained by using EBSD 3D orientation data (Prior et al., 1999), collected in the Geochemical Analysis Unit (GAU), Macquarie University on a Zeiss IVO SEM (Scanning Electron Microscopy) with a Nordlys Nano High sensitivity EBSD detector and an X-Max EDS detector to ensure a high quality EBSD and chemical data. The latter data was needed to ensure correct identification of different feldspars. Analysis conditions were high vacuum, 20 kV acceleration voltage, beam current of 8.0 mA, and at a working distance of ~12 mm. The chosen step size was 15 μm. Grains are defined as areas completely surrounded by high angle boundaries (misorientation ≥10°). Only grains that are constituted by at least 4 data points are considered. Boundaries with misorientations of 2-10° are defined as subgrain boundaries (Trimby et al., 2000; Warren and Hirth, 2006; Pearce et al., 2011). Grains with an average internal misorientation <1° are considered as strain-free (Piazolo et al., 2006). Noise reduction on the raw data followed methods tested by Prior et al. (2002), Bestmann & Prior (2003), and Piazolo et al. (2006). Orientations are plotted in equal area, lower hemisphere pole figures (one point per grain), half width 20° and cluster size 5° to investigate the presence and/or absence of crystallographic preferred orientation (CPO) (Law, 1990; Menegon et al., 2011). Misorientation axes (MXD) data are shown in equal area and upper hemisphere inverse pole figures, and the axes value divided by valid grain (>65 μm) amounts (i.e. MXD axes/grain amounts ratio, see Table 1 for detail) will be used to detect mineral's deformation degree. Misorientation angle distributions (MAD) are presented for neighbour and random pairs (also known as correlated and uncorrelated data, N=1000 for random pairs). In addition, another microstructural parameter GOS (grain orientation spread) which represents average deviation of the orientation of a measurement point from the average orientation of the grain (cf. Wright et al. (2011) for a review), is also computed. Considering the geological conditions and samples' properties, we concentrated our analysis on plagioclase, K-feldspar and hornblende (>10%) in each domain (i.e. residuum or neosome). Additionally, we used J-index for the minerals' long <c> axis as a measure for CPO strength and computed the average angle of the long grain shape axis relative to the foliation plane. The GOS and J-index data sets are calculated by using MTEX, the Matlab toolbox by using orientation data from EBSD (Mainprice et al., 2011, 2014).

4. Results

4.1. Field relationships and general sample description

The metatexite sample comes from the east side of Shawanzi (N:40°54’03”, E: 110°04’10”; Figure 1). In outcrop this gneiss is dipping northward and exhibits a large number of 0.5-1.5 m wide, felsic veins (Figures 1b and 2a), banded gneiss (tonalite with granitic injection; Figure 2b) and stromatic to net migmatitic structure (Figure 2c). The diatexite are collected near Xuehaigou in the southern part of the study area (N:40°37’32”, E: 110°06’05”; Figure 1), where felsic migmatites are exposed and characterized by 3-5 cm wide felsic (feldspars and quartz) bands (Figure 2d). The local gneiss is injected by mafic dykes (now metamorphosed to mafic granulite with subsequent melt injections; Figure 2d). The felsic migmatite in this area exhibits flow structures (e.g. schlieren structures) surrounding rigid mafic blocks (Figures 2e and 2f).

4.2. Microstructural characteristics in migmatites

In the metatexite plagioclase (66.5%) is the dominant mineral of the residuum. The grains are equigranular with an equant grain shape, curved grain boundaries and are also polygonal with abundant 120° triple junctions (Figures 4a and 5a). The average grain size is 186 μm with a low mineral aspect ratio (1.56) (Table 1). Hornblende grains in residuum exhibit a shape preferred orientation (Figure 3a). The grain sizes are in various (porphyroclast or anhedral grain shapes; Figures 3a and 5b) with some intergrain brittle fractures (Figure 4b). Consequently, the total grain size variation is large while rare porphyroblasts (>500 μm; 5 grains) exist and smaller grains dominate the whole domain (Figures 3a and 5a and Table 1). In hornblende abundant areas, equilibrium triple junctions are frequent, minor biotite locally occurs at hornblende boundaries

(Figure 4b). The average aspect ratio of hornblende (1.78) is significantly higher than plagioclase (Table 1). For the subordinate minerals, K-feldspar grains are dispersed in the residuum domain with subhedral shapes, quartz grains exhibit banded shapes and occur mainly as interstitial material (Figure 6a). Plagioclase in the neosome domain shows a similar grain size range, shape, and aspect ratio as in the residuum, except that the mean grain size is smaller (162 μm), K-feldspar in the neosome has similar features as plagioclase (Table 1 and Figures 4c and 6a) in the same domain. Myrmekite is seen adjacent to plagioclase (Figure 4a). The hornblende is also present in the neosome and surrounded by plagioclase clusters (Table 1 and Figures 4c, 6a and 6e). Quartz has a low abundance (less than 5%; Table 1) in two domains and either forms bands (Figure 5a) or occurs as interstitial grains surrounded by feldspars (Figures 4a and 6e).

The diatexite reveals more complicated microstructural relationships. The residuum plagioclase grains have grain sizes of 166 μm, generally euhedral shape with some straight grain boundaries (Figures 3b and 4d and Table 1). K-feldspar grains take up 15% of the residuum, hence are higher in abundance than that in the metatexite's residuum, and exhibit smaller grain size (122 μm). Grains occur evenly distributed with euhedral or rounded shapes among plagioclase (Table 1 and Figure 7a). Quartz shows either rounded inclusions around plagioclase grains (Figure 4d) or bands across plagioclase grains (Figures 7a). In neosome domain, plagioclase grains are seen in grain clusters with curved grain boundaries, some of which have 120° triple junctions (Figures 4e and 4f). The average value of plagioclase in the neosome is around 175 μm, hence between residuum and neosome in the metatexite but the aspect ratio is larger with 1.71 (Table 1). K-feldspar's grain size and aspect ratio are lower than plagioclase (Table 1). Hornblende's aspect ratio is clustered with an average of 1.81, the porphyroblasts are common (33 grains) and exhibit a relatively higher aspect ratio (2.03) (Table 1). Hornblende commonly has euhedral shapes, and the average grain size is almost two times larger than that in the metatexite's residuum (Figures 3b, 4e, 4f and 8a and Table 1). Quartz exhibits different shapes forming narrow bands, or appear as rounded inclusions (Figures 4e, 4f and 8a) while K-feldspar occurs in multi-grain aggregates (Figure 8a). Biotite is rare in the neosome domain (Figure 8a).

Additionally, it is necessary to be noted that no core-mantle structures are seen in either of the two samples. The main constituent minerals of each domain exhibit similar average long-axis orientation (Table 1).

4.3. Quantitative crystallographic orientation analysis and microstructural data

4.3.1. Metatexite (16BT28-11)

In the residuum, plagioclase grains show that the [100] axis is parallel to lineation, while plane (010) and (001) are weakly parallel to foliation (Figure 5b). In MAD diagrams, plagioclase's correlated data have a relatively high frequency in the low angle area (0-50° area) and similar distribution as theoretical curve in uncorrelated data (Figure 5c). For misorientation axes, they are clustered near [-100] direction, the intersecting point between (010) and (100) planes (Figure 5d). For hornblende, (100) plane are parallel to the foliation and the [001] directions are parallel to the lineation. MAD diagram also illustrates higher frequency in the low the angle area (0-50°, especially in 0-10° area) for correlated data, while uncorrelated data demonstrates a weak bimodal distribution with higher distribution tendency in the low angle area, misorientation axes distribution is converged on [001], and some axes are centered around [100] (Figures 5b-d). Both plagioclase and hornblende's GOS values and average long axes angles to horizontal direction are similar, and the angles are coincide with the [100] (plagioclase) and [001] (hornblende) directions in pole figures, but hornblende has much larger MXD axes/grain amount ratio and J-index than plagioclase (Table 1 and Figure 5b). Plagioclase exhibits abundant subgrain boundaries in EBSD phase and grain map (Figure 5e), which is also shown in individual grains as clear intracrystalline lattice bending (Figure 9a). Similar subgrain boundaries (or undulatory distinction) is also shown in micrographs (Figure 4a). Hornblende grains exhibit subgrain boundaries and preserve some intracrystalline deformation from grain center to rim (Figures 5e and 9a).

Plagioclase grains in neosome illustrate similar EBSD data (pole figures, MAD and MXD figures) as within the residuum while plane (001) has a more foliation-parallel tendency than plane (010). MAD diagram for random-pairs reveals a weak bimodal distribution and a high frequency of neighbor-pairs is seen for medium angles (40-50° area). The misorientation axes distribution tends to be concentrated between [-100] and [201], with (010) and (001) planes intersection (Figures 6b-d). Plane (010) in K-feldspar aligns with foliation and axis [100] with lineation (Figure 6b). In MAD diagram the mineral has a weak bimodal distribution (random-pairs), and relatively high frequency in 0-50° range in both neighbour- and random-pairs (including 0-10° in neighbour-pairs; Figure 6c). For the misorientation axes, K-feldspar are around [001] direction mainly and [100] as secondary maximum, and MXD axes/grain amount ratio in plagioclase is higher than K-feldspar (Table 1 and Figure 6d). Feldspars have similar GOS, J-index and angle from horizontal to mineral long axis (Table 1 and Figure 6b). Both feldspars demonstrate a certain amount of subgrain boundaries in EBSD phase and grain map (Figure 6e), their individual plagioclase grains also exist similar deformation characteristics (subgrain boundaries in 2-5° range; Figure 9a). Plagioclase's long axis and pole figure direction are more accordant than K-feldspar (Table 1 and

Figures 6b and 6e). K-feldspar dominates the neosome domain (much lower Pl/Kfs ratio than residuum; Table 1 and Figure 6a), while the total abundance of 2-10° misorientation axes is less than plagioclase (Figure 6d), even if some K-feldspar grains exhibit strong internal crystal lattice bending (Figure 9a).

4.3.2. Diatexite (16BT14-3)

Plagioclase in the residuum domain exhibits (001) plane sub-parallel to foliation, most [100] directions are parallel to lineation (Figure 7b). The MAD is similar to that seen for the metatexite's neosome, however, there is higher frequency in both neighbour- and random-pairs in several ranges (0-10°, 30-90°, 140-160°) (Figure 7c). The intracrystalline deformation of plagioclase grains is obviously lower than metatexite's domains (fewer subgrain boundaries, lower M/G values and misorientation changes; Figures 7d and 9b). K-feldspar's CPO is non-random with plane (001) parallel to foliation (Figure 7b). The K-feldspar MAD diagram shows high frequency for 0-20°, 40-60° and 80-90° ranges in random-pairs data and high frequency in 0-40°, 70-110° and 130-150° ranges for neighbour-pairs data (Figure 7c). 2-10° misorientation axes shows a dominance of the [001] axis (Figure 7d). Both of the two feldspars' low-angle misorientation axes are much less (70 in plagioclase and 48 in K-feldspar), and so is the MXD axes/grain amount ratio (K-feldspar is larger than plagioclase) (Figure 7d). Feldspar grains have similar GOS, long axis angles to the main foliation (15.61° and 18.02°) and higher J-indices (13.4 and 10.7) (Table 1 and Figure 7b). In the neosome, the plagioclase CPO is characterized by [100] axis parallel to lineation, while planes (010) and (001) are weakly parallel to foliation, hence is similar to that of the residuum in the metatexite (Figure 8b). In the MAD diagram, plagioclase's neighbour-pairs data have higher frequency than theoretical at low-to medium angles (0-60°) (Figure 8c). The misorientation axes distribution is clustered between [-100] and [201] direction but the axis number is much less than previous sample's residuum (Figure 8d). For individual grains, not only much fewer subgrain boundaries exist, but also lower misorientation degree (mostly lower than 2°; Figure 9b). K-feldspar has similar less pronounced CPO to that of the metatexite's neosome. The MAD demonstrates high frequency in 0-80° (neighbour-pairs) range, 0-10° angles show a higher frequency than in theory and are more pronounced than for plagioclase. The misorientation axes distribution is almost the same as the one in metatexite's neosome domain while the axis number is only about half of that domain (176 pts) (Figures 8b-d). Hornblende's (100) and (010) planes are coupled as seen on a pole figure similar to the metatexitie's residuum with direction [001] parallel to lineation with the alignment of [001] being more pronounced than that of (010) (Figure 8b). MAD neighbour-pair data has a higher frequency than theoretical for angles of 0-70°, 0-10° angles area is much higher than theoretical but are not as pronounced as in the metatexite. Misorientation axes are randomly distributed and the amount is less than half of metatexite's residuum (338 pts) (Figures 8b-d). Internal deformation of hornblende shows that there is significant crystal bending close to grain edges while the center of grains reveals little intracrystalline deformations. (Figure 9b). Three minerals have similar long axis angle, the accordance between the angle and pole figure, MXD axes/grain amount ratio and J-index are increasing from plagioclase, K-feldspar to hornblende, and random-pairs data in neosome's three minerals are all in accordance with theoretical curve, GOS in K-feldspar is higher than in plagioclase but lower than in hornblende (Table 1 and Figures 8b-d). Finally, all plagioclase MAD diagrams are strongly influenced by common twins (Figures 5c, 6c, 7c and 8c).

5. Discussion

5.1. Identification of phases during migmatisation

Felsic minerals such as quartz, plagioclase and potassium feldspar are usually considered as previous melt in the anatexites (Sawyer, 1999, 2001; Hasalová et al., 2008; Lee et al., 2017). Accordingly, we suggest that the neosome domains in the two migmatites represent areas of high melt presence during the migmatisation event (Sawyer & Brown, 2008). Field relationship shows that diatexite outcrops have more obvious anatectic flowing textures than metatexite outcrops (Figure 2).

The estimated neosome percentage in the two respective outcrops (not including later injected veins) in diatexite is much higher than in metatexite, supported by both hand specimen and microscale observation of the two studied samples (Figure 3 and Table 1). In residuum domain, both K-feldspar and quartz grains in selected samples are aggregated (Figures 5a and 7a) or in the case of quartz form inclusions or bands (Figures 4a, 4d and 4f), we suggest that in the residuum melt might still have existed at such conditions (i.e. K-feldspar and quartz represent the in-situ melted mineral in residuum). The two migmatites' selected neosome domains have different modal contents (Table 1), quartz in these domains has either rounded or banded shape in these domains (more obvious in diatexite; Figures 4e, 4f, 6a and 8a). K-feldspar in metatexite (54.5%) and plagioclase in diatexite (29.7%) are the main felsic minerals in the neosome domain and show lower crystal plastic deformation features (such as low 2-10° misorientation axes/grain amount ratio, GOS value and abundance of internal deformation; Table 1 and Figures 6d, 8d and 9) than the minerals in residuum domains. In the neosome domain, K-feldspar in metatexite has weaker deformation than plagioclase, and plagioclase in diatexite has weaker deformation than K-feldspar

(Table 1 and Figures 6d, 8d and 9). We suggest that these weakly deformed minerals were initially melted during the peak of the migmatisation event and recrystallized from the melt later (Figures 6a and 8a; Pakrash et al. 2018), rounded grains in the neosome might be the new-generated melt before the last final melt frozen (Figures 4c, 4e and 6e). Neosome's solid phase in syn-melt condition is either residuum's rock mass (plagioclase in metatexite) or restite surrounded by dominantly melt (K-feldspar in diatexite). These minerals experience deformation in both prior to and after partial melting condition, so that their deformation characteristics are stronger than those developed at post-melt condition only (Table 1 and Figure 9). Therefore, these minerals can be introduced as a reference to divide solid and liquid phase in the syn-melt condition. Accordingly, considering K-feldspar and quartz as the melt phases in the metatexite's neosome, plagioclase and quartz in the diatexite's neosome, the melted areas in the two samples are ~25% in the metatexite and ~50% in the diatexite (Table 1).

The two migmatites exhibit features in the field and under the microscope that are markedly influenced by melt, which separates the period before the melt presence and after the melting period. Deformation characteristics in different rocks allow us to identify which characteristics are typical for the rock in the three main periods of its evolution, namely pre-, syn- and post-melt. Due to the neosome domains in two migmatites all reveal different deformation degrees in different minerals, we infer that in neosome, minerals with weaker deformation characteristics belong to liquid phase during syn-melt condition, and the post-melt deformation is weaker than pre-melt condition. Based on this discovery, the dominant deformation progress in residuum took place in pre-melt condition. In summary, the residuum represents mainly the pre-melt situation, especially for the diatexite, where we suggest that based on field relationships and the composition of the observed neosome is largely externally derived. At syn-melt conditions, minor partial melting occurred in residuum and the rock was fluxed by derived melt (usually mixed up with solid rock). For the diatexite, partial melting was more pronounced. The post-melt situation is represented by both residuum and neosome's "frozen" microstructure (Table 2 and Figure 10). In the following section, we would discuss the detailed microstructural evolution in pre- (residuum only), syn- (mostly neosome) and post-melt (mostly neosome) conditions.

5.2. Deformation conditions and mechanisms of migmatite's residuum and neosome

5.2.1. Pre-melt condition and deformation mechanisms

In metatexite, plagioclase has equant grains (Figure 5a), and frequent subgrain boundaries and their axes (or misorientation axes distributions) represents the existence of (001) [100] CPO, pointing to the importance of dislocation creep and thus power-law creep behavior (Figures 5d, 5e and 9a and Table 2; Marshall & Mclaren, 1977; Kruse et al., 2001; Ji et al., 2004). For hornblende grains (Figures 4b, 5a and 5e) subgrain misorientation axes are clustered near the [001] direction. (100) [001] is inferred as the main slip system for the hornblende in this domain (Figures 5b; Díaz Aspiroz et al., 2007; Getsinger & Hirth, 2014). In addition, low-angle neighbour-pairs data (0-10°) is extremely in high frequency, confirming significant intracrystalline deformation in the hornblende (Figures 5c, 5e and 9a). Accordingly, we believe that dislocation creep plays an essential role in the hornblende deformation during pre-melt condition. The absence of core-mantle textures and numerous curved grain boundaries (Figures 4a and 5a) is consistent with high temperature deformation where grain boundary migration (GBM) plays a significant role (Table 2; Rosenberg & Stünitz, 2003; Passchier & Trouw, 2005). K-feldspar has weaker CPO

(Figure 7b) but higher GOS and M/D value than plagioclase (Table 1 and Figure 7d), supports our interpretation that this mineral was mostly deformed during the pre-melt condition. MXD has similar distribution to K-feldspar in other domains, which also indicate dislocation creep (Figure 7d; Ishii et al., 2007). However, some component of crystal plastic deformation is suggestion by the fact that the [001] direction closer to Y axis in pole figure and higher MXD axes/grain amount ratio suggest that lattice orientation was not so accordant as in other domains (Bestmann & Prior, 2003; Table 1 and Figure 7b).

Plagioclase in diatexite has a similar curved grain shape as in the metatexite (Figures 4d, 4f and 7a), but exhibits a more prominent CPO, suggesting dominance of the (001) [100] slip system. The field outcrops show that diatexite are more influenced by ductile shearing in higher temperature (Figures 2d-f; Cai, Liu, Liu, Liu, et al., 2013, Cai, Liu, Liu, Shi & Liu, 2013, Cai et al., 2014), consequently, CPO and J-index are much stronger (Table 1 and Figure 7b). The simultaneous lower frequency of subgrain boundaries suggests that GBM in plagioclase was more pronounced leading to a decrease in the number of subgrains (Figure 4d and Table 2; Urai et al., 1986; Passchier & Trouw, 2005).

5.2.2. Syn-melt condition and deformation mechanisms

By microstructural observation, the residuum in two migmatites have all experienced partial melting, which are characterized by randomized oblate quartz and/or K-feldspar aggregates (Figures 4a, 4d, 5a and 7a), the diatexite's residuum has a larger melt mineral content than the metatexite's (Table 1). Photomicrographs and EBSD maps of the metatexites' neosome show that it is strongly aligned to the foliation (Figures 3a and 5a), which suggests that melt migration was syntectonic (Sawyer, 2001). Plagioclase in neosome has similar deformation characteristics to that in the residuum (Figures 6d, 6e and 9a), and small hornblende grains are present in the neosome's plagioclase aggregate (Figures 4c, 6a and 6e). We suggest that these areas originate from the residuum and form remnant "islands" within the melt injection dominated neosome. Based on the fact that K-feldspar has weaker deformation characteristics than plagioclase, we suggest that it represents a significant part of the melt that injected the residuum during melt present deformation (Table 2 and Figure 10).

In the diatexite's neosome, plagioclase is randomly and irregularly distributed (Figure 8a), suggesting that it crystallized out at the veining stages of migmatisation (Sawyer, 2001; Stuart et al., 2018). The signatures of internal deformation (MXD axes/grain amount ratio, GOS, J-index in Table 1 and intracrystalline deformation features in Figure 9b) are more pronounced in hornblende and K-feldspar suggest stronger deformation than plagioclase. We infer that the hornblende and K-feldspar form clear phenocrysts in the neosome; the hornblende has almost two times the average grain size than that in metatexite's residuum (Table 1 and Figure 8a). It also exhibits a euhedral shape with felsic inclusions and very little recrystallization features (Figures 4e, 8a and 9b). Such characteristics can be attributed to a peritectic reaction, considering the granulite facies condition (Busch et al., 1974; Weinberg & Hasalova, 2015; Hu et al., 2016). Hornblende is well oriented with high aspect ratio, and the orientation tendency (long-axis angle) is similar to [001] direction (i.e. the coherent SPO (shape preferred orientation) and CPO; Table 1 and Figures 8a and 8b), accompanied with near random MAD (random-pair, similar distribution to theoretical) and strain-free internal structures of hornblende grains (Figures 8c and 9b), these features are consistent with rigid body rotation in a constricted flow, with dissolution-precipitation creep

(Berger & Stunitz, 1996; Imon et al., 2004; Díaz Aspiroz et al., 2007). Although the gneissosity of diatexite is not as obvious as in the metatexite, the banded quartz also illustrate parallel-to-lineation tendency (Figures 4e, 4f and 8a), hence suggest syn-tectonic migmatisation (Figure 10). Rheologically, for both the metatexite and diatexite, the flow properties of the bulk rock would have been dominated by the properties of the melt, suggesting Newtonian flow at overall lower viscosities than at pre- and post- melt conditions (Table 2; e.g. Champallier et al., 2008).

5.2.3. Post-melt condition and deformation mechanisms

Overall, for metatexite, there is very little evidence both in the outcrops and at the thin section scale of the retrogression due to the later exhumation; only in some places hornblende grains are replaced by biotite in the residuum (Figures 4b and 5a and Table 2). This replacement, however, could be due to H_2O-rich fluids expelled by the crystallizing melt facilitating the growth of a high temperature biotite at near peak metamorphic conditions (Speer, 1987; Kriegsman, 2001). Hence, post-melt features are interpreted to be representative of lower crustal processes. In metatexite's neosome, K-feldspar exhibits some subgrains that related to the activation of a high-temperature slip system (Figures 6d and 6e). The subgrain boundaries in the K-feldspar imply that dislocation creep took over as the dominant deformation mechanism after melt frozen, however, the low frequency of subgrain boundaries and lower GOS value in the K-feldspar in the neosome suggest that the finite strain taken up was minor (Tables 1 and 2 and Figures 6d and 6e). K-feldspar in this domain exhibits activation of the (010) [100] slip system (Figure 6b; Martelat et al., 1999). Both residuum and neosome's feldspars have well developed 120° triple junctions (Figures 4c, 5a and

6a), which may be due to annealing (static recrystallization) process after melt crystallized (Flinn, 1969; Dallain et al., 1999; Smith et al., 2015).

It is striking that within the residuum in diatexite, an extremely high J-index, as is seen for plagioclase (Table 1 and Figure 7b). This may suggest that the finer grained plagioclase in residuum took up most of the deformation not only pre- but also post-migmatisation (Figure 10). Although high J-index might due to the limited grain numbers, which might overestimate the value (Ben Ismaïl and Mainprice, 1998), considering K-feldspar also has finer grain size, its high J-index is probably also by similar mechanism. In the diatexite's neosome, the crystallized plagioclase exhibits crystal bending and recrystallization by GBM (Figure 8a and Table 2) and shows similar but weaker CPO and subgrain boundary axes distribution as in other domains (Figures 8b and 8d). This phenomenon also implies that the deformation progress in post-melt condition is weaker than pre-melt condition. K-feldspar shows irregular boundaries suggesting GBM (Figure 8a and Table 2). The CPO ((010) [100]) and misorientation axes distributions are similar to that in the metatexite's neosome (Figures 6b and 6d), suggesting some influence of dislocation creep. For individual grains of hornblende, both (100) [001] and (010) [001] were activated with random MXD (Figures 8b and 8d; Díaz Aspiroz et al., 2007; Getsinger & Hirth, 2014), so the "subgrain boundaries" might be considered as healed cracks (Danner et al., 2019) in post-melt condition, they are much fewer and mostly around the grains' rims, most core areas of the hornblende grains are strain-free (Figure 9b), suggesting that the late stage deformation took place at the rim of the grains. According to the information mentioned above, we infer that these deformation features of the K-feldspar and hornblende were produced dominantly at post-melt condition (Figure 10).

Overall, during post-migmatisation, deformation was dominated by dislocation creep with possible strain localization into the residuum area, the larger grain size in neosome results in minor deformation in that area (Tables 1 and 2 and Figure 10). This interpretation is supported by the fact that the narrow residuum domain usually has smaller grain size, stronger CPO and higher aspect ratio, GOS value, J-index and aligned biotite (Table 1 and Figures 6b and 7b), which all point to higher strain (or strain rate) (Rybacki & Dresen, 2004; Warren & Hirth, 2006; Morales and Tommasi, 2011; Hansen et al., 2014; Mainprice et al., 2014). The reason why plagioclase in the two diatexite domains has similar aspect ratios might be due to the final annealing process (Table 2).

5.3. Implications for lower crustal rheology

Based on the previous discussion, the following rheological evolution can be derived (Table 2 and Figure 10). During pre-melt condition, power-law (i.e. dislocation creep) dominates the two migmatites' residuum. Once syn-melt condition started, Newtonian melt flow dominated the rheology of the both rocks (especially in neosome) as both exhibit a melt fraction significantly above 50% melt (by calculating total melted minerals in Table 1; Lejeune & Richet, 1995; Burg & Vigneresse, 2002; Rosenberg & Handy 2005; Champallier et al., 2008), with viscosities significantly lower than the other two evolutionary stages. During post-melt condition when unescaped melt was totally crystallized in situ, grain sizes are larger in the neosome and low strain is accommodated by dislocation creep with a power-law stress–strain rate relationship. However, post-migmatisation deformation features are subtle hence we interpret that the rocks experienced only minor deformation, deeming it relatively hard rheologically.

6. Predicted seismic signals of the lower crust during pre-, syn- and post-migmatisation

6.1. Method

To calculate the seismic properties we used the MTEX and MSAT toolbox based on Matlab utilizing the orientation data from EBSD analysis (Mainprice et al., 2011, 2014; Walker & Wookey, 2012; Lee et al., 2017). Elastic moduli of related minerals at ambient conditions were used (Aleksandrov & Ryzhova, 1961; McSkimin et al., 1965; Aleksandrov et al., 1974), while the melt's elastic moduli are based on Rivers & Carmichael (1987). Since we consider a polymineralic assemblage, we used the Voigt-Reuss-Hill average tensor method (Hill, 1952; Mainprice, 1990). We calculate seismic velocities for pre-, syn- and post-melt conditions taking data from different parts of the rock into account. Data from the residuum domain is used to simulate the pre-melt conditions. For syn-melt conditions, data from the residuum without partial melt and the minerals interpreted to have been present as a solid within the melt (now neosome) are used. Considering the melt in neosome play a main role in this period, we simulated 60% melt in metatexite's neosome and 50% melt in diatexite's neosome, which were similar to the percentage of melted minerals in their individual domain (Table 1). The minor partial melting process in residuum domains were not considered in this case study. The melt simulation process was calculated using the MSAT toolbox, modelled as oblate shaped melt inclusion (the aspect ratio is 10:10:1) based on Lee et al. (2017). For post-melt conditions data from the whole rock is utilized (see Figure 11 for detail). The volume fractions of minerals in different conditions were based on EBSD data shown in Table 1: pre-melt condition shows dominant mineral without partial melting in residuum only (plagioclase and hornblende in metatexite, plagioclase, K-feldspar and biotite in diatexite), syn-melt condition shows a combination of valid minerals in residuum mentioned above, identified as solid phase in neosome (plagioclase and hornblende in metatexite, K-feldspar and hornblende in diatexite) and melt (the volume is same as the minerals identified as melt in neosome, K-feldspar and quartz in metatexite, plagioclase and quartz in diatexite), post-melt condition shows whole rock (see Figure 11). Rock density in different domains was calculated based on the volume fractions of minerals (minerals lower than 1% in each domain were not considered, see Table 1). The elastic constants of samples in different situations are provided in the supporting information (Table S1). The seismic figures' orientation is also similar to pole figures, foliation parallel to XY position, lineation parallel to X direction.

6.2. Seismic calculations - General trends

In the metatexite, the magnitude of P-wave velocities and most seismic anisotropies are similar but higher pre-melt than post-melt conditions, while shear wave seismic anisotropies in melting condition are the highest, shear wave velocity and Vp/Vs ratios are similar in these two conditions (Table 3 and Figure 11). For the syn-melt condition, seismic velocities are lower, seismic anisotropies are far greater than observed pre- and post-melt. Syn-melt maximum Vp/Vs ratios are higher than observed pre- and post-melt, while minimum Vp/Vs ratios are closer to those conditions (Table 3). By observing seismic figures, in pre-melt condition, maximum P-wave velocity is sub-parallel to the X axis and minimum zone is sub-parallel to YZ plane, maximum S-wave anisotropies are concentrated on XY plane (i.e. foliation plane), Vs_1 maximum zones have a similar distribution while Vs_2 maximum zones are near the primitive circle and minimum zones are clustering around the YZ plane, and Vs_1 polarization is parallel to foliation (XY plane; Figure

11a). While in post-melt (melt frozen) condition, P-wave's minimum zone is sub-parallel to YZ plane to Z direction, moreover, S-wave anisotropy and two shear wave velocity figures' high value (or low value) zones are cross-like, consequently, similar to P-wave, Vs_1 polarization is also disturbed but the general directions are not influenced (Figure 11a). The syn-melt condition is different to previous two conditions (Figure 11a): the first three figures' (Vp, AVs and Vs_1) high-value areas are parallel and close to XY plane, Vs_1 polarization is parallel to XY plane in high-value area but randomly in low-value area, Vs_2's high-value zones are shown as girdles along the ~45° direction to X axis.

In diatexite, the magnitude of all seismic velocity data (Vs) are lower, while all anisotropic and Vp/Vs data are higher in pre- than post-melt condition, the data in syn-melt condition is similar to metatexite (Table 3). Although the selected minerals in three conditions are different, diatexite's seismic properties do not vary a lot between pre- and post-melt conditions (Figure 11b). The felsic mineral dominant residuum domain has the maximum Vp oriented approximately parallel to lineation, while the minimum Vp direction is slightly inclined (~15°) relative to the foliation. S-wave anisotropy's two maximum clusters are almost in symmetry by YZ plane, the Vs_1 polarization is mostly normal except in the lower part of seismic figures which are subvertical to XY plain. Vs_1 also have two maximum clusters parallel to XY plane, Vs_2 maximum zones are around the base circle, ~45° to X or Z direction and the minimum zones are around X or Z direction. For the post-melt condition, the distribution of Vp is similar to residuum. A higher S-wave anisotropy (AVs) zone is distributed along the foliation plain and the Vs_1 distribution and polarization in the high anisotropy zones tends to parallel to XY plane. The maximum Vs_2 zone is similar to the residuum and minimum zone is along the YZ plane. The syn-melt condition is also similar to metatexite (Figure 11b).

6.3. Seismic properties of the lower crust at different conditions

The calculated seismic signals give valuable information to infer changes in response to the geological evolution (i.e. state at different conditions). In the following we examine the changes in magnitude of seismic properties for each of the different conditions and discuss these in the light of the literature.

For seismic velocity magnitude, there is a clear correlation between the existence of hornblende and fast Vp. In the metatexite Vp is faster than domains that exhibit low percentage of hornblende (i.e. pre-melt conditions in metatexite; Tables 3 and 4 and Figure 11; Tatham et al., 2008; Lloyd et al., 2011). As a result, for pre-melt condition, the metatexite has higher seismic velocities than diatexite. For syn-melt conditions, the seismic velocities decrease (Table 3). Typically, larger melt fractions lead to greater seismic velocity reduction (Hammond & Humphreys, 2000; Lee et al., 2017), in this case study, the metatexite with a lower melt fraction has a greater reduction in seismic velocity (Tables 3 and 4). In addition, regardless of the different melt fractions and distributions, the two migmatites have similar seismic figures (Figure 11); their profiles are also similar to results produced for 20% melt distributed as oblate ellipsoids by Lee et al. (2017). The maximum shear wave velocity in the two migmatites is consistent with geophysical lower crust simulations that show Vs is usually lowest at 20-30 km depth followed by an increase at lower depths (Caldwell et al., 2009; Hacker et al., 2014; Ferri et al., 2016).

After the melt crystallizes, the seismic velocities of the two migmatites are increased by migmatite solidification (Tables 3 and 4 and Figure 11). The addition of felsic frozen melt increases the metatexite's P-wave velocity, and the dominant hornblende in final diatexite increases the seismic velocities (Tatham et al., 2008; Lloyd et al., 2011). By observing seismic velocity distribution (except for the Vs_2) there is a striking change in the pattern of seismic velocities of the metatexite at post-melt condition relative to the pre-melt condition (Figure 11a). Since K-feldspar is the dominant mineral in neosome (and second largest percentage in the whole rock) while little is present in the residuum, it is probably the key factor responsible for the observed seismic signals. For diatexite, although modal contents in residuum (dominant in pre-melt condition) and neosome (dominant in post-melt condition) are different, these two conditions have accordant seismic profiles (Figure 11b). Such distribution is probably attributed to biotite in residuum and hornblende in neosome (Kern et al., 2009; Lloyd et al., 2011).

Within the diatexite seismic anisotropy is strongly related to the presence and alignment of the biotite seen within the residuum accounting for higher seismic anisotropies than in the metatexite domains (Tables 3 and 4 and Figure 11; Lloyd et al., 2011; Ferré et al., 2014). Once in the melt present (syn-melt) condition, both two migmatites' seismic anisotropies are much greater (Tables 3 and 4 and Figure 11). Almqvist et al. (2015) and Ferri et al. (2016) conducted experiments measuring seismic anisotropy at high temperatures (>700 °C) and the AVp values could be as high as 15-20%. In this case study, however, the minimum seismic anisotropy could be as high as 37%. For AVs, the value is coincided with Lee et al. (2017)'s result in migmatitic samples. Regardless of different melt fractions and distributions, in syn-melt conditions, either melt-injection (metatexite) or melt flowing (diatexite) process lead to extreme-high seismic anisotropies, and Vs_1 polarization in high areas is parallel to foliation.

After melt crystallization, the magnitude of the two migmatites' seismic anisotropies decrease

(Tables 3 and 4), following suggestions that decreasing temperature and felsic melt crystallization is expected to decrease seismic anisotropy (Ferri et al., 2016; Lee et al., 2017). The AVs seismic anisotropy figures of metatexite and diatexite in post-melt condition's distribution are similar in pattern to the pre-melt conditions (Figure 11).

Generally, if no big difference in modal content, the Vp/Vs ratios in two migmatites are similar in two non-melt conditions (Tables 3 and 4). In syn-melt condition, they have high maximum Vp/Vs ratios and diatexite is even higher (Table 3). In geophysical review, the high Vp/Vs (e.g. >2; Julià et al., 2005) is considered as partial molten crust (Nabelek et al., 2009; Xie et al., 2013; Hacker et al., 2014; Ferri et al., 2016). In addition, Hacker et al. (2014) also indicate that rock with deeper partial molten in lower crust have higher Vp/Vs ratio. Considering diatexite were melt-dominant in syn-melt condition, so at least in this case study, Vp/Vs ratio is more coincided with melt fraction than seismic velocity.

Conclusions

The microstructural and crystallographic orientation evolution of typical examples of lower crustal migmatites enables us to identify the active deformation mechanisms, their rheology and their seismic characteristics. Using the differences between different domains of the rock, we determine the likely characteristics of the lower crust deformation at high temperatures either in a solid state or during melt presence or after a migmatisation event.

In pre-melt condition, the tonalitic host rock deforms by dislocation creep at high temperature (>700 ℃) including grain boundary migration recrystallization where the phases governing the deformation behavior are hornblende and plagioclase. Hence at these conditions the rheology would show a power-law stress-strain rate relationship. Seismic signatures of these rocks are characterized by high P-wave velocity.

At melt present conditions and melt percentages above 10% produced either by partial melting (in residuum) or through injection of externally derived melt (the later neosome), deformation is dominantly taken up by the melt phase, leaving the residuum and floating phenocrysts and residuum-remnants largely in a rigid state. Rheologically this rock has a significantly lower viscosity than its non-melt counterpart and a rheological behavior approaching Newtonian flow. The seismic signal is characterized by lower seismic velocities, higher maximum Vp/Vs ratios and extremely high seismic anisotropies, regardless of different melt fractions and distributions. High melt fraction coincides with high maximum Vp/Vs ratio.

At post-melt lower crustal condition, the previous felsic melt in syn-melt condition crystallized as coarse-grained material. Natural examples of such rocks suggest that even though ductile deformation may continue the bulk strain taken up by the “frozen-in” migmatite is low. Solid state deformation is also dominated by high temperature dislocation creep resulting in a power-law creep behavior. In these rocks the microstructures are well equilibrated (i.e. frequent equilibrium triple junctions), hence high temperature, low strain grain boundary adjustment at high temperatures commonly referred to as annealing must play a major role in the post-migmatisation period. Locally some strain localization within for example biotite rich, softer diatexite’s residuum may be seen. Migmatites with “frozen felsic melt” lead to significant lower seismic velocities, anisotropies, and maximum Vp/Vs ratios than the signatures of melt present condition. If the migmatite had similar modal content to its residuum, even if experienced the influence of frozen melt, it could also preserve similar seismic properties to pre-melt condition.

Although some of these discoveries contradict previous research, they supply a new view to lower crust research, and the melt simulation separate the migmatite's syn-melt period from solid status, which might be meaningful for the following research.

Acknowledgments

This project was financially supported by the National Natural Science Foundation of China (Grant No. 41772212, 41872215, 41230206), academic scholarship and oversea academic communication funding project of Jilin University, China Scholarship Council (Grant No. 201708250002), Taishan Scholars (Grant No. ts20190918), Qingdao Leading innovation talents project (Grant No. 19-3-2-19-zhc) and Zhufeng Project funded by Ocean University of China together. YS is grateful to Liene Spruzeniece and Uvana Meek, Macquarie University for their help with SEM-based EBSD analysis, and to Duo Zhang from College of Earth Sciences, Jilin University, Jonathan Griffin from Department of Geology, University of Otago for proofreading and language help. We are also grateful to Bo Zhang and one anonymous reviewer for their valuable suggestions, as well as Editor Ulrich Faul for paper handling. All data and scripts are available via the DOI https://doi.pangaea.de/10.1594/PANGAEA.907560

References:

Aleksandrov, K., Alchikov, U., Belikov, B., Zaslavskii, B., & Krupnyi, A. (1974). Velocities of elastic waves in minerals at atmospheric pressure and increasing precision of elastic constants by means of EVM. *Izv. Acad. Sci. USSR, Geol. Ser, 10*, 15-24.

Aleksandrov, K., & Ryzhova, T. (1961). Elastic properties of rock-forming minerals II: Layered silicates. *Bulletin of the Academy of Sciences of the USSR Geophysics Series, English translation, 12*, 1165-1168.

Almqvist, B. S. G., & Mainprice, D. (2017). Seismic properties and anisotropy of the continental crust: Predictions based on mineral texture and rock microstructure. *Reviews of Geophysics*. doi: 10.1002/2016rg000552

Almqvist, B. S. G., Misra, S., Klonowska, I., Mainprice, D., & Majka, J. (2015). Ultrasonic velocity drops and anisotropy reduction in mica-schist analogues due to melting with implications for seismic imaging of continental crust. *Earth and Planetary Science Letters, 425*, 24-33. doi: 10.1016/j.epsl.2015.05.039

Barker, F., & Arth, J. G. (1976). Generation of trondhjemitic-tonalitic liquids and Archean bimodal trondhjemite-basalt suites. *Geology*, *4*(10), 596-600.

Barker, F., Arth, J. G., & Hudson, T. (1981). Tonalites in crustal evolution. *Philosophical Transactions of the Royal Society of London. Series A, Mathematical and Physical Sciences*, *301*(1461), 293-303.

Ben Ismaïl, W., & Mainprice, D. (1998). An olivine fabric database an overview of upper mantle fabrics and seismic anisotropy. *Tectonophysics, 296*, 145-157.

Berger, A., & Stünitz, H. (1996). Deformation mechanisms and reaction of hornblende: examples from the Bergell tonalite (Central Alps). *Tectonophysics, 257*, 149-174.

Bestmann, M., & Prior, D. J. (2003). Intragranular dynamic recrystallization in naturally deformed calcite marble: diffusion accommodated grain boundary sliding as a result of subgrain rotation recrystallization. *Journal of Structural Geology, 25*(10), 1597-1613. doi: 10.1016/s0191-8141(03)00006-3

Burg, J. P., & Vigneresse, J. L. (2002). Non-linear feedback loops in the rheology of cooling-crystallizing felsic magma and heating-melting felsic rock. *Geological Society, London, Special Publications, 200*(1), 275-292.

Bürgmann, R., & Dresen, G. (2008). Rheology of the Lower Crust and Upper Mantle: Evidence from Rock Mechanics, Geodesy, and Field Observations. *Annual Review of Earth and Planetary Sciences, 36*(1), 531-567. doi: 10.1146/annurev.earth.36.031207.124326

Burov, E. B., & Diament, M. (1995). The effective elastic thickness (T e) of continental lithosphere: What does it really mean? *Journal of Geophysical Research: Solid Earth, 100*(B3), 3905-3927.

Busch, W., Schneider, C., & Mehnert, K. R. (1974). Initial melting at grain boundaries. Part II: Melting in rocks of granodioritic, quartzdioritic and tonalitic composition. *Neues Jahrb. Mineral. Mh.,* 8, 345-370.

Cai, J., Liu, F., Liu, P., Liu, C., Wang, F., & Shi, J. (2014). Metamorphic P–T path and tectonic implications of pelitic granulites from the Daqingshan Complex of the Khondalite Belt, North China Craton. *Precambrian Research, 241,* 161-184. doi: 10.1016/j.precamres.2013.11.012

Cai, J., Liu, F., Liu, P., Shi, J., & Liu, J. (2013a). Petrogenesis and metamorphic P-T conditions of garnet-spinel-biotite-bearing paragneiss in Danangou area, Daqingshan-Wulashan metamorphic complex belt [in Chinese with English abstract]. *Acta Petrologica Sinica, 29*(7), 2313-2328.

Cai, J., Liu, P., Liu, F., Liu, J., Wang, F., & Shi, J. (2013b). Genetic mineralogy and metamorphic evolution of Al-rich gneisses in the Shiguai area, Daqingshan-Wulashan metamorphic complex belt [in Chinese with English abstract]. *Acta Petrologica Sinica, 29*(2), 437-461.

Caldwell, W. B., Klemperer, S. L., Rai, S. S., & Lawrence, J. F. (2009). Partial melt in the upper-middle crust of the northwest Himalaya revealed by Rayleigh wave dispersion. *Tectonophysics, 477*(1-2), 58-65. doi: 10.1016/j.tecto.2009.01.013

Champallier, R., Bystricky, M., & Arbaret, L. (2008). Experimental investigation of magma rheology at 300 MPa: From pure hydrous melt to 76 vol.% of crystals. *Earth and Planetary Science Letters, 267*(3-4), 571-583. doi: 10.1016/j.epsl.2007.11.065

Cooper, R. F., & Kohlstedt, D. L. (1984). Solution-precipitation enhanced diffusional creep ofpartially molten olivine-basalt aggregates during hot-pressing. *Tectonophysics, 107*, 207-233.

Cyprych, D., Piazolo, S., & Almqvist, B. S. G. (2017). Seismic anisotropy from compositional banding in granulites from the deep magmatic arc of Fiordland, New Zealand. *Earth and Planetary Science Letters, 477*, 156-167. doi: 10.1016/j.epsl.2017.08.017

Dallain, C., Schulmann, K., & Ledru, P. (1999). Textural evolution in the transition from subsolidus annealing to melting process, Velay Dome, French Massif Central. *Journal of Metamorphic Geology, 17*, 61-74.

Danner, T., Hjorth Jakobsen, U., & Geiker, M. R. (2019). Mineralogical sequence of self-healing products in cracked marine concrete. *Minerals, 9*(5), 284.

Dell'Angelo, L. N., & Tullis, J. (1988). Experimental deformation of partially melted granitic aggregates. *Journal of Metamorphic Geology, 6*, 495-515.

Díaz Aspiroz, M., Lloyd, G. E., & Fernández, C. (2007). Development of lattice preferred orientation in clinoamphiboles deformed under low-pressure metamorphic conditions. A SEM/EBSD study of metabasites from the Aracena metamorphic belt (SW Spain). *Journal of Structural Geology, 29*(4), 629-645. doi: 10.1016/j.jsg.2006.10.010

Dong, C., Wan, Y., Wilde, S. A., Xu, Z., Ma, M., Xie, H., & Liu, D. (2014). Earliest Paleoproterozoic supracrustal rocks in the North China Craton recognized from the Daqingshan area of the Khondalite Belt: Constraints on craton evolution. *Gondwana Research, 25*(4), 1535-1553.

Ferré, E. C., Gébelin, A., Conder, J. A., Christensen, N., Wood, J. D., & Teyssier, C. (2014). Seismic anisotropy of the Archean crust in the Minnesota River Valley, Superior Province. *Geophysical Research Letters, 41*(5), 1514-1522.

Ferri, F., Burlini, L., & Cesare, B. (2016). Effect of partial melting on Vp and Vs in crustal enclaves from Mazarrón (SE Spain). *Tectonophysics, 671*, 139-150. doi: 10.1016/j.tecto.2015.12.030

Flinn, D. (1969). Grain contacts in crystalline rocks. *Lithos, 3*, 361-370.

Franěk, J., Schulmann, K., & Lexa, O. (2006). Kinematic and rheological model of exhumation of high pressure granulites in the Variscan orogenic root: example of the Blanský les granulite, Bohemian Massif, Czech Republic. *Mineralogy and Petrology, 86*(3-4), 253-276. doi: 10.1007/s00710-005-0114-4

Franěk, J., Schulmann, K., Lexa, O., Ulrich, S., Štípská, P., Haloda, J., & Týcová, P. (2011). Origin of felsic granulite microstructure by heterogeneous decomposition of alkali feldspar and extreme weakening of orogenic lower crust during the Variscan orogeny. *Journal of Metamorphic Geology, 29*(1), 103-130. doi: 10.1111/j.1525-1314.2010.00911.x

Getsinger, A. J., & Hirth, G. (2014). Amphibole fabric formation during diffusion creep and the rheology of shear zones. *Geology, 42*(6), 535-538. doi: 10.1130/g35327.1

Gómez Barreiro, J., Martínez Catalán, J. R., Prior, D., Wenk, H. R., Vogel, S., Díaz García, F., . . .

Lonardelli, I. (2010). Fabric Development in a Middle Devonian Intraoceanic Subduction Regime: The Careón Ophiolite (Northwest Spain). *The Journal of Geology, 118*(2), 163-186. doi: 10.1086/649816

Gong, W., Hu, J., Wu, S., Chen, H., Qu, H., Li, Z., . . . Wang, L. (2014). Possible southwestward extrusion of the Ordos Block in the Late Paleoproterozoic: Constraints from kinematic and geochronologic analysis of peripheral ductile shear zones. *Precambrian Research, 255*, 716-733. doi: 10.1016/j.precamres.2014.05.001

Guernina, S., & Sawyer, E. W. (2003). Large-scale melt-depletion in granulite terranes: an example from the Archean Ashuanipi Subprovince of Quebec. *Journal of Metamorphic Geology, 21*, 181-201.

Guo, J., Peng, P., Chen, Y., Jiao, S., & Windley, B. F. (2012). UHT sapphirine granulite metamorphism at 1.93–1.92Ga caused by gabbronorite intrusions: Implications for tectonic evolution of the northern margin of the North China Craton. *Precambrian Research*, *222-223*, 124-142. doi: 10.1016/j.precamres.2011.07.020

Hacker, B. R., Ritzwoller, M. H., & Xie, J. (2014). Partially melted, mica-bearing crust in Central Tibet. *Tectonics, 33*, 1408-1424. doi: 10.1002/

Hammond, W. C., & Humphreys, E. D. (2000). Upper mantle seismic wave velocity: Effects of realistic partial melt geometries. *Journal of Geophysical Research: Solid Earth*, *105*(B5), 10975-10986. doi: 10.1029/2000jb900041

Hansen, L. N., Zhao, Y. H., Zimmerman, M. E., & Kohlstedt, D. L. (2014). Protracted fabric evolution in olivine: Implications for the relationship among strain, crystallographic fabric, and seismic anisotropy. *Earth and Planetary Science Letters, 387*, 157-168. doi:

10.1016/j.epsl.2013.11.009

Hasalová, P., Schulmann, K., Lexa, O., Štípská, P., Hrouda, F., Ulrich, S., . . . Týcová, P. (2008). Origin of migmatites by deformation-enhanced melt infiltration of orthogneiss: A new model based on quantitative microstructural analysis. *Journal of Metamorphic Geology, 26*(1), 29-53.

Hill, R. (1952). The elastic behaviour of a crystalline aggregate. *Proceedings of the Physical Society A, 65*, 349-354.

Holtzman, B. K., & Kendall, J. M. (2010). Organized melt, seismic anisotropy, and plate boundary lubrication. *Geochemistry, Geophysics, Geosystems, 11*(12), doi:10.1029/2010gc003296

Hu, Z.P., Zhang, Y.S., Hu, R., Wang, J., Siebel, W., & Chen, F. (2016). Amphibole-bearing migmatite in North Dabie, eastern China: Water-fluxed melting of the orogenic crust. *Journal of Asian Earth Sciences, 125*, 100-116.

Imon, R., Okudaira, T., & Kanagawa, K. (2004). Development of shape- and lattice-preferred orientations of amphibole grains during initial cataclastic deformation and subsequent deformation by dissolution–precipitation creep in amphibolites from the Ryoke metamorphic belt, SW Japan. *Journal of Structural Geology, 26*(5), 793-805. doi: 10.1016/j.jsg.2003.09.004

Ishii, K., Kanagawa, K., Shigematsu, N., & Okudaira, T. (2007). High ductility of K-feldspar and development of granitic banded ultramylonite in the Ryoke metamorphic belt, SW Japan. *Journal of Structural Geology, 29*(6), 1083-1098. doi:10.1016/j.jsg.2007.02.008

Jackson, J. (2002). Strength of the continental lithosphere: time to abandon the jelly sandwich? *GSA Today, 12,* 4-9.

Ji, S., Jiang, Z., Rybacki, E., Wirth, R., Prior, D., & Xia, B. (2004). Strain softening and microstructural evolution of anorthite aggregates and quartz–anorthite layered composites deformed in torsion. *Earth and Planetary Science Letters*, *222*(2), 377-390. doi: 10.1016/j.epsl.2004.03.021

Jin, W., Li, S., & Liu, X. (1991). A study on characteristics of early Precambrian high-grade metamorphic rock series and their metamorphic dynamics [in Chinese with English abstract]. *Acta Petrologica Sinica*, *4*, 27-35.

Jin, W., Li, S., & Liu, X. (1992). Early Precambrian metamorphic rocks and early earth crust evolution in Daqingshan, Inner Mongolia [in Chinese with English abstract]. *Journal of Changchun University of Earth Sciences, 22*(3), 281-289.

Johannes, W., & Gupta, L.N. (1982). Origin and evolution of a migmatite. *Contributions to Mineralogy and Petrology, 79*(2), 114-123.

Julià, J., Mancilla, F., & Morales, J. (2005). Seismic signature of intracrustal magmatic intrusions in the Eastern Betics (Internal Zone), SE Iberia. *Geophysical Research Letters*, *32*(16).

Jung, S., & Hellebrand, E. (2006). Trace element fractionation during high-grade metamorphism and crustal melting—constraints from ion microprobe data of metapelitic, migmatitic and igneous garnets and implications for Sm–Nd garnet chronology. *Lithos*, *87*(3-4), 193-213.

Kern, H., Mengel, K., Strauss, K., Ivankina, T., Nikitin, A., & Kukkonen, I. (2009). Elastic wave velocities, chemistry and modal mineralogy of crustal rocks sampled by the Outokumpu scientific drill hole: Evidence from lab measurements and modeling. *Physics of the Earth and Planetary Interiors*, *175*(3-4), 151-166.

Kretz, R. (1983). Symbols for rock-forming minerals. *American Mineralogist*, *68*(1-2), 277-279.

Kriegsman, L. M. (2001). Partial melting, partial melt extraction and partial back reaction in anatectic migmatites. *Lithos*, *56*, 75-96.

Kriegsman, L. M., & Hensen, B. J. (1998). Back reaction between restite and melt implications for geothermobarometry and pressure-temperature paths. *Geology, 26*(12), 1111-1114.

Kruse, R., Stünitz, H., & Kunze, K. (2001). Dynamic recrystallization processes in plagioclase porphyroclasts. *Journal of Structural Geology, 23*, 1781-1802.

Lamarque, G., Bascou, J., Maurice, C., Cottin, J.-Y., Riel, N., & Ménot, R.-P. (2016). Microstructures, deformation mechanisms and seismic properties of a Palaeoproterozoic shear zone: The Mertz shear zone, East-Antarctica. *Tectonophysics, 680,* 174-191. doi: 10.1016/j.tecto.2016.05.011

Law, R. D. (1990). Crystallographic fabrics: a selective review of their applications to research in structural geology. *Geological Society, London, Special Publications, 54*(1), 335-352. doi: 10.1144/gsl.sp.1990.054.01.30

Lee, A. L., Walker, A. M., Lloyd, G. E., & Torvela, T. (2017). Modeling the impact of melt on seismic properties during mountain building. *Geochemistry*, *Geophysics*, *Geosystems*, *18*, 1-21. doi: 10.1002/

Lejeune, A. M., & Richet, P. (1995). Rheology of crystal-bearing silicate melts: An experimental study at high viscosities. *Journal of Geophysical Research: Solid Earth, 100*(B3), 4215-4229. doi: 10.1029/94jb02985

Li, S., Sun, D., Yu, H., Jin, W., Liu, X., & Cao, L. (1995). *Distribution of ductile shear zones and metallogenic prediction of the related gold deposits in the early Precambrian metamorphic rocks, mid-western Inner Mongolia* [in Chinese]. Changchun: Scientific and technical publishing of Jilin.

Lloyd, G. E., Butler, R. W. H., Casey, M., Tatham, D., & Mainprice, D. (2011). Constraints on the seismic properties of the middle and lower continental crust. *Geological Society, London, Special Publications, 360*(1), 7-32.

Ma, M., Dong, C., Xu, Z., Xie, S., Liu, D., & Wan, Y. (2015). Anatexis of Early Paleoproterozoic garnet-biotite gneisses (Daqingshan supracrustal rocks) in Daqingshan, Inner Mongolia: Geology, zircon geochronology and geochemistry. *Acta Petrologica Sinica, 31*(06), 1535-1548.

Ma, M., Wan, Y., Santosh, M., Xu, Z., Xie, H., Dong, C., . . . Guo, C. (2012). Decoding multiple tectonothermal events in zircons from single rock samples: SHRIMP zircon U–Pb data from the late Neoarchean rocks of Daqingshan, North China Craton. *Gondwana Research, 22*(3–4), 810-827. doi: http://dx.doi.org/10.1016/j.gr.2012.02.020

Ma, M., Wan, Y., Xu, Z., Liu, S., Xie, H., Dong, C., & Liu, D. (2012). Late Paleoproterozoic K-feldspar pegmatite vein in the Daqingshan area, North China Craton: SHRIMP age and Hf composition of zircons. *Geological Bulletin of China, 31*(6), 825-833.

Mainprice, D. (1990). A FORTRAN program to calculate seismic anisotropy from the lattice preferred orientation of minerals. *Computers & Geosciences*, *16*(3), 385-393.

Mainprice, D., Bachmann, F., Hielscher, R., Schaeben, H., & Lloyd, G. E. (2014). Calculating anisotropic piezoelectric properties from texture data using the MTEX open source package. *Geological Society, London, Special Publications, 409*(1), 223-249. doi: 10.1144/sp409.2

Mainprice, D., Hielscher, R., & Schaeben, H. (2011). Calculating anisotropic physical properties from texture data using the MTEX open-source package. *Geological Society, London, Special Publications, 360*(1), 175-192. doi: 10.1144/sp360.10

Marshall, D. B., & McLaren, A. C. (1977). Deformation mechanisms in experimentally deformed plagioclase feldspars. *Physics and Chemistry of Minerals, 1*, 351-370.

Martelat, J. E., Schulmann, K., Lardeaux, J. M., Nicollet, C., & Cardon, H. (1999). Granulite microfabrics and deformation mechanisms in southern Madagascar. *Journal of Structural Geology, 21*, 671-687.

McSkimin, H., Andreatch Jr, P., & Thurston, R. (1965). Elastic moduli of quartz versus hydrostatic pressure at 25 and− 195.8 C. *Journal of Applied Physics, 36*(5), 1624-1632.

Menegon, L., Piazolo, S., & Pennacchioni, G. (2011). The effect of Dauphiné twinning on plastic strain in quartz. *Contributions to Mineralogy and Petrology, 161*(4), 635-652. doi: 10.1007/s00410-010-0554-7

Miranda, E. A., & Klepeis, K. A. (2016). The interplay and effects of deformation and crystallized melt on the rheology of the lower continental crust, Fiordland, New Zealand. *Journal of Structural Geology, 93*, 91-105. doi: 10.1016/j.jsg.2016.09.007

Morales, L. F. G., & Tommasi, A. (2011). Composition, textures, seismic and thermal anisotropies of xenoliths from a thin and hot lithospheric mantle (Summit Lake, southern Canadian Cordillera). *Tectonophysics, 507*(1-4), 1-15. doi: 10.1016/j.tecto.2011.04.014

Nabelek, J., Hetenyi, G., Vergne, J., Sapkota, S., Kafle, B., Jiang, M., . . . Hi, C. T. (2009). Underplating in the Himalaya-Tibet collision zone revealed by the Hi-CLIMB experiment. *Science, 325*(5946), 1371-1374. doi: 10.1126/science.1167719

Olsen, S. N. (1977). Origin of the Baltimore gneiss migmatites at Piney Creek, Maryland. *Geological Society of America Bulletin, 88*(8), 1089-1101.

Passchier, C. W., & Trouw, R. A. J. (2005). *Microtectonics. 2nd.* Berlin: Springer-verlag.

Paterson, M. S. (2001). A granular flow theory for the deformation of partially molten rock. *Tectonophysics, 335*, 51-61.

Pearce, M. A., Wheeler, J., & Prior, D. J. (2011). Relative strength of mafic and felsic rocks during amphibolite facies metamorphism and deformation. *Journal of Structural Geology, 33*(4), 662-675. doi:10.1016/j.jsg.2011.01.002

Piazolo, S., Bestmann, M., Prior, D. J., & Spiers, C. J. (2006). Temperature dependent grain boundary migration in deformed-then-annealed material: Observations from experimentally deformed synthetic rocksalt. *Tectonophysics, 427*(1-4), 55-71. doi: 10.1016/j.tecto.2006.06.007

Prakash, A., Piazolo, S., Saha, L., Bhattacharya, A., Pal, D. K., & Sarkar, S. (2018). Deformation behavior of migmatites: insights from microstructural analysis of a garnet–sillimanite–mullite–quartz–feldspar-bearing anatectic migmatite at Rampura–Agucha, Aravalli–Delhi Fold Belt, NW India. *International Journal of Earth Sciences*. doi: 10.1007/s00531-018-1598-6

Prior, D. J., Boyle, A. P., Brenker, F., Cheadle, M. C., Day, A., Lopez, G., . . . Zetterstrom, L. (1999). The application of electron backscatter diffraction and orientation contrast imaging in the SEM to textural problems in rocks. *American Mineralogist, 84*, 1741-1759.

Prior, D. J., Wheeler, J., Peruzzo, L., Spiess, R., & Storey, C. (2002). Some garnet microstructures an illustration of the potential of orientation maps and misorientation analysis in microstructural studies. *Journal of Structural Geology, 24*, 999-1011.

Rivers, M. L., & Carmichael, I. S. (1987). Ultrasonic studies of silicate melts. *Journal of Geophysical Research: Solid Earth, 92*(B9), 9247-9270.

Rosenberg, C. L., & Handy, M. R. (2005). Experimental deformation of partially melted granite revisited: implications for the continental crust. *Journal of Metamorphic Geology, 23*(1), 19-28. doi: 10.1111/j.1525-1314.2005.00555.x

Rosenberg, C. L., & Stünitz, H. (2003). Deformation and recrystallization of plagioclase along a temperature gradient an example from the Bergell tonalite. *Journal of Structural Geology*, *25*, 389-408.

Rudnick, R. L., & Fountain, D. M. (1995). Nature and composition of the continental crust: a lower crustal perspective. *Reviews of Geophysics, 33*(3), 267-309.

Rybacki, E., & Dresen, G. (2004). Deformation mechanism maps for feldspar rocks. *Tectonophysics*, *382*(3-4), 173-187. doi: 10.1016/j.tecto.2004.01.006

Santosh, M., Sajeev, K., Li, J. H., Liu, S. J., & Itaya, T. (2009). Counterclockwise exhumation of a hot orogen: The Paleoproterozoic ultrahigh-temperature granulites in the North China Craton. *Lithos, 110*(1-4), 140-152. doi: 10.1016/j.lithos.2008.12.010

Santosh, M., Tsunogae, T., Li, J. H., & Liu, S. J. (2007). Discovery of sapphirine-bearing Mg–Al granulites in the North China Craton: Implications for Paleoproterozoic ultrahigh temperature metamorphism. *Gondwana Research, 11*(3), 263-285. doi: 10.1016/j.gr.2006.10.009

Sawyer, E. W. (1999). Criteria for the recognition of partial melting. *Physics and Chemistry of the Earth*, *24*(3), 269-279.

Sawyer, E. W. (2001). Melt segregation in the continental crust: distribution and movement of melt in anatectic rocks. *Journal of Metamorphic Geology, 19*, 291-309.

Sawyer, E. W. (2008). *Atlas of migmatites* (Vol. 9). Ottawa: NRC Research press.

Sawyer, E. W. (2014). The inception and growth of leucosomes: microstructure at the start of melt segregation in migmatites. *Journal of Metamorphic Geology, 32*(7), 695-712. doi: 10.1111/jmg.12088

Sawyer, E. W., & Brown, M. (Eds). (2008). *Working with migmatites* (Vol. 38): Mineralogical Assn of Canada.

Sawyer, E. W., Cesare, B., & Brown, M. (2011). When the Continental Crust Melts. *Elements, 7*(4), 229-234. doi:10.2113/gselements.7.4.229

Schilling, F. R., & Partzsch, G. M. (2001). Quantifying partial melt fraction in the crust beneath the central Andes and the Tibetan Plateau. *Physics and Chemistry of the Earth, Part A: Solid Earth and Geodesy, 26*(4), 239-246.

Smith, J. R., Piazolo, S., Daczko, N. R., & Evans, L. (2015). The effect of pre-tectonic reaction and annealing extent on behaviour during subsequent deformation: insights from paired shear zones in the lower crust of Fiordland, New Zealand. *Journal of Metamorphic Geology, 33*(6), 557-577. doi: 10.1111/jmg.12132

Speer, J. A. (1987). Evolution of magmatic AFM mineral assemblages in granitoid rocks; the hornblende+ melt= biotite reaction in the Liberty Hill Pluton, South Carolina. *American Mineralogist*, *72*(9-10), 863-878.

Stuart, C. A., Daczko, N. R., & Piazolo, S. (2017). Local partial melting of the lower crust triggered by hydration through melt-rock interaction: an example from Fiordland, New Zealand. *Journal of Metamorphic Geology, 35*(2), 213-230. doi: 10.1111/jmg.12229

Stuart, C. A., Meek, U., Daczko, N. R., Piazolo, S., & Huang, J. X. (2018). Chemical Signatures of Melt–Rock Interaction in the Root of a Magmatic Arc. *Journal of Petrology, 59*(2), 321-340. doi: 10.1093/petrology/egy029

Tatham, D. J., Lloyd, G. E., Butler, R. W. H., & Casey, M. (2008). Amphibole and lower crustal seismic properties. *Earth and Planetary Science Letters, 267*(1-2), 118-128. doi: 10.1016/j.epsl.2007.11.042

Trimby, P. W., Drury, M. R., & Spiers, C. J. (2000). Recognising the crystallographic signature of recrystallisation processes in deformed rocks: a study of experimentally deformed rocksalt. *Journal of Structural Geology, 22*(11-12), 1609-1620.

Tuttle, O. F., & Bowen, N. L. (1958). Origin of Granite in the Light of Experimental Studies in the System $NaA1Si_3O_8$-$KA1Si_3$-H_2O. *Geological Society of America.*

Urai, J. L., Means, W. D., & Lister, G. S. (1986). Dynamic recrystallization of minerals. In *Mineral and rock deformation: laboratory studies* (Vol. 36, pp. 161-199). Washington, DC: AGU.

Vanderhaeghe, O. (2001). Melt segregation, pervasive melt migration and magma mobility in the continental crust: the structural record from pores to orogens. *Physics and Chemistry of the Earth, Part A: Solid Earth and Geodesy, 26*(4), 213-223.

Vanderhaeghe, O., & Teyssier, C. (2001). Partial melting and flow of orogens. *Tectonophysics, 342,* 451-472.

Venables, J., & Harland, C. (1973). Electron back-scattering patterns—a new technique for obtaining crystallographic information in the scanning electron microscope. *Philosophical Magazine, 27*(5), 1193-1200.

Walker, A. M., & Wookey, J. (2012). MSAT—A new toolkit for the analysis of elastic and seismic anisotropy. *Computers & Geosciences, 49,* 81-90.

Walte, N. P., Bons, P. D., & Passchier, C. W. (2005). Deformation of melt-bearing systems—insight from in situ grain-scale analogue experiments. *Journal of Structural Geology, 27*(9), 1666-1679. doi: 10.1016/j.jsg.2005.05.006

Wan, Y., Liu, D., Dong, C., Xu, Z., Wang, Z., Wilde, S. A., ... & Zhou, H. (2009). The Precambrian Khondalite Belt in the Daqingshan area, North China Craton: evidence for multiple metamorphic events in the Palaeoproterozoic era. *Geological Society, London, Special Publications, 323*(1), 73-97.

Wan, Y., Xu, Z., Dong, C., Nutman, A., Ma, M., Xie, H., . . . Cu, H. (2013). Episodic Paleoproterozoic (∼2.45, ∼1.95 and ∼1.85 Ga) mafic magmatism and associated high temperature metamorphism in the Daqingshan area, North China Craton: SHRIMP zircon U–Pb dating and whole-rock geochemistry. *Precambrian Research, 224*, 71-93. doi: http://dx.doi.org/10.1016/j.precamres.2012.09.014

Warren, J. M., & Hirth, G. (2006). Grain size sensitive deformation mechanisms in naturally deformed peridotites. *Earth and Planetary Science Letters, 248*, 438-450. doi: 10.1016/j.epsl.2006.06.006

Weinberg, R. F., & Hasalová, P. (2015). Water-fluxed melting of the continental crust: A review. *Lithos, 212-215*, 158-188. doi: 10.1016/j.lithos.2014.08.021

Wright, S. I., Nowell, M. M., & Field, D. P. (2011). A review of strain analysis using electron backscatter diffraction. *Microscopy and microanalysis, 17*(3), 316-329.

Xie, J., Ritzwoller, M. H., Shen, W., Yang, Y., Zheng, Y., & Zhou, L. (2013). Crustal radial anisotropy across Eastern Tibet and the Western Yangtze Craton. *Journal of Geophysical Research: Solid Earth, 118*(8), 4226-4252. doi: 10.1002/jgrb.50296

Xu, Z., Liu, Z., Yang, Z., Wu, X., & Chen, X. (2007). Structure of metamorphic strata of the khondalite series in the Daqingshan-Wulashan area, central Inner Mongolia, China, and their geodynamic implications [in Chinese with English abstract]. *Geological Bulletin of China, 26*(5), 526-536.

Xu, Z., Wan, Y., Dong, C., Ma, M., & Liu, D. (2015). Late Neoarchean magmatism identified in

Daqingshan, Inner Mongolia: SHRIMP zircon U-Pb dating [in Chinese with English abstract]. *Acta Petrologica Sinica, 31*(6), 1509-1517.

Yang, Z., Xu, Z., Liu, Z., & Huang, D. (2008). *Geological investigation and research on high-grade metamorphic regions* [in Chinese]. Beijing: Geological Publication House.

Závada, P., Schulmann, K., Konopásek, J., Ulrich, S., & Lexa, O. (2007). Extreme ductility of feldspar aggregates—Melt-enhanced grain boundary sliding and creep failure: Rheological implications for felsic lower crust. *Journal of Geophysical Research, 112*(B10). doi: 10.1029/2006jb004820

Závada, P., Schulmann, K., Racek, M., Hasalová, P., Petr, J., Weinberg, R. F., . . . Roberts, A. (2018). Role of strain localization and melt flow on exhumation of deeply subducted continental crust. *Lithosphere, 10*(2), 217-238.

Zhao, G. (2007). When did plate tectonics begin on the North China Craton Insights from metamorphism. *Earth Science Frontiers, 14*(1), 19-32.

Zhao, G., Cawood, P. A., Li, S., Wilde, S. A., Sun, M., Zhang, J., . . . Yin, C. (2012). Amalgamation of the North China Craton: Key issues and discussion. *Precambrian Research, 222-223*, 55-76. doi: 10.1016/j.precamres.2012.09.016

Zhao, G., & Guo, J. (2012). Precambrian geology of China: preface. *Precambrian Research, 222*, 1-12.

Zhao, G., Sun, M., Wilde, S. A., & Li, S. (2005). Late Archean to Paleoproterozoic evolution of the North China Craton: key issues revisited. *Precambrian Research, 136*(2), 177-202.

Zhao, G., Wilde, S. A., Cawood, P. A., & Sun, M. (2002). SHRIMP U–Pb zircon ages of the Fuping Complex: implications for late Archean to Paleoproterozoic accretion and assembly of the North China Craton. *American Journal of Science, 302*(3), 191-226

Tables:

Table 1

General Information of the Two Studied Tonalitic Migmatites. Total Rock-forming Minerals Stand For Minerals in One Sample's All Measured Domains (Percentages Mean Total Mineral Modal Content), Modal Percent and Feldspars' Ratio, Valid Grain Amounts, Grain Size, Aspect Ratio, GOS, J-index, Angle between Long Axis and Horizontal, MXD Axis Amounts and MXD Axes/grain Amounts Ratio Information are All Based on EBSD data, Hornblende's Microstructural Data inside Brackets Represent Porphyroblastic Grains (larger than 500 μm). Mineral Abbreviations Used Follow Kretz (1983).

Anatectic type	Total rock-forming minerals	EBSD measured domain	Mineral	Modal percent %	Pl/Kfs ratio	Number of grains	Average grain size d/μm	Aspect ratio	GOS/°	J-index	Angle between long axis and horizontal/°	MXD axis	MXD axes/grain amount
Metatexite (16BT28-11)	Pl (58.0%) Kfs (21.7%) Hb (14.3%) Q (3.5%) Bt (2.5%)	Residuum (70%)	Pl	66.5	9.64	758	186	1.56	0.75	3.15	-4.76	1239	1.63
			Kfs	6.9									
			Hb	20.0		352 (5)	148 (657)	1.78 (2.10)	0.73	9.34	-7.11	743	2.11
			Q	3.2									
			Bt	3.4									
		Neosome (30%)	Pl	39.5	0.72	252	162	1.69	0.58	7.91	-0.79	466	1.85
			Kfs	54.5		300	176	1.65	0.55	6.49	0.27	300	1.00
			Hb	1.6									
			Q	4.4									
Diatexite (16BT14-3)	Pl (32.4%) Kfs (13.8%)	Residuum (15%)	Pl	64.1	4.27	221	166	1.69	0.43	13.4	15.61	70	0.32
			Kfs	15.0		74	122	1.59	0.46	10.7	18.02	48	0.65
			Q	11.8									
			Bt	9.1									

Hb (33.8%)		Pl	29.7		519	175	1.71	0.33	4.09	21.34	153	0.29
		Kfs	13.5		309	149	1.65	0.51	4.79	21.09	176	0.57
Q (18.3%)	Neosome (85%)	Hb	37.8	2.20	214 (33)	257 (743)	1.81 (2.03)	0.4	8.51	21.09	338	1.58
Bt (1.7%)		Q	18.9									

Abbreviations: Bt: biotite; Hb: hornblende; Kfs: K-feldspar; Pl: plagioclase; Q: quartz.

Table 2

Overall Deformation and Rheological Characteristics of Two Migmatites in Different Melting Periods

Rock type	Characteristics	Pre-melt	Syn-melt		Post-melt
		Residuum	Residuum	Neosome (with crystalline material in melt)	residuum and neosome
Metatexite	General microstructures	Both plagioclase and hornblende have numerous subgrain boundaries. Plagioclase has euhedral grains while hornblende has anhedral grains.	Similar to pre-melt condition.	Plagioclase (with minor hornblende) has similar characteristic as that in residuum, and surrounded by K-rich melt.	K-feldspar grains in neosome were equant, and the grain shape was similar to plagioclase in both domains. Some additional subgrain boundaries, and straight grain boundaries with 120° triple junctions were generated in feldspars in two domains, some hornblende grains in residuum were accompanied by biotite.

	Deformation mechanism	Minerals experienced dominant dislocation creep（GBM in plagioclase) with some subgrain formation in high temperature.	Dislocation creep was stopped, K-feldspar and quartz were in melt status.	Plagioclase should be originally from residuum and keeps similar microstructural characteristics.	Dislocation creep (GBM) and subsequent annealing process were added in two feldspars in both domains.
	Rheological distribution	Power-law behavior dominant.	Largely rigid with minor melt flow.	Rheology dominanted by melt (Newtonian).	power-law, weaker than pre-melt condition, strain localization might be existed in restricted neosome.
Diatexite	General microstructures	Plagioclase grains are equant and curved in high temperature, with much fewer subgrain boundaries.	Similar to that in metatexite, the melting degree was higher.	K-feldspar and hornblendes were crystallized in this period, hornblende had larger grain size than in metatexite, they are surrounded by dominant melt. These solid phases might preserve minor earlier deformation features.	In residuum, feldspars have lower grain size and fewer subgrain boundaries than neosome, accompanied with straight grain boundaries and 120° triple junctions. In neosome, feldspars experienced similar process like in metatexite's neosome and the grain shapes are more curved, K-feldspar has stronger deformation characteristics than plagioclase, and subgrain boundaries in hornblende are mostly existed in rim area.

Deformation mechanism	Main dislocation creep (GBM), which might be erased by later partial melting process in high temperature.	Very little deformation with melt inhabitation.	Little deformation in this period, hornblende was influenced by rigid body rotation with dissolution-precipitation creep, hornblende result of peritectic reaction.	Hornblende experienced minor deformation fracturing and healing of fractures, K-feldspar exhibit irregular grain boundaries, deformation by GBM; less pronounced in plagioclase.
Rheological distribution	Power-law behavior dominant.	Softer than metatexite's residuum but harder than neosome, the restricted melt flow is stronger than matatexite's residuum.	Similar to metatexite, with higher strain due to dominant melt flowing (Newtonian) with low viscosity.	Power-law, rheologically weaker than pre-melt condition, but stronger than metatexite, strain localization might existed in restricted residuum.

Table 3

Seismic Velocities, Anisotropies, and Velocity ratios of Anatectic Migmatites in Different Melting Conditions (Pre-melt: Residuum Domain Only; Syn-melt: Residuum and Crystallized Minerals in Leucosome/melanosome; Post-melt: Residuum and Leucosome/melanosome Domains).

Rock type	Condition	Vp_max (km/s)	Vp_min (km/s)	Vs_1_max (km/s)	Vs_1_min (km/s)	Vs_2_max (km/s)	Vs_2_min (km/s)	Max Vp Anisotropy	Max Vs Anisotropy	Max Vs_1 Anisotropy	Max Vs_2 Anisotropy	Vp/Vs_1 max	Vp/Vs_1 min	Vp/Vs_2 max	Vp/Vs_2 min
Metatexite	Pre-melt	6.30	5.99	3.35	3.23	3.28	3.20	5.1	4.2	3.9	2.5	1.89	1.83	1.96	1.85
	Syn-melt	5.49	3.77	2.92	1.42	2.30	1.41	37.2	69.4	68.8	48.0	2.66	1.68	3.88	1.89
	Post-melt	6.23	5.96	3.31	3.20	3.29	3.19	4.5	3.5	3.4	3.0	1.89	1.80	1.95	1.84
Diatexite	Pre-melt	6.15	5.48	3.34	2.97	3.10	2.86	10.5	14.3	11.7	7.9	1.94	1.74	2.15	1.82
	Syn-melt	5.88	3.88	3.20	1.43	2.45	1.40	41.0	78.1	76.3	55.0	2.73	1.62	4.22	1.84
	Post-melt	6.49	6.04	3.64	3.48	3.53	3.45	7.2	5.1	4.4	2.4	1.81	1.72	1.87	1.74

Table 4

Seismic Signatures of Two Migmatites in Different Melting Periods

Rock type	Seismic characteristics		
	Pre-melt	Syn-melt	Post-melt (compare to pre-melt)
Metatexite	Hornblende lead to higher P-wave velocities.	Obvious lower seismic velocities and higher maximum Vp/Vs ratio, seismic anisotropies have a huge increase and seismic figures have extremely changes.	Vp, AVs and Vs_1 parameters decreased, Vp/Vs kept similar values to residuum, most seismic figures changed with crystallized neosome added.
Diatexite	Felsic rock characteristics.	Similar to metatexite.	Seismic velocities and anisotropies were decreased, Vp/Vs were decreased. Minor changes in seismic figures.

Figures:

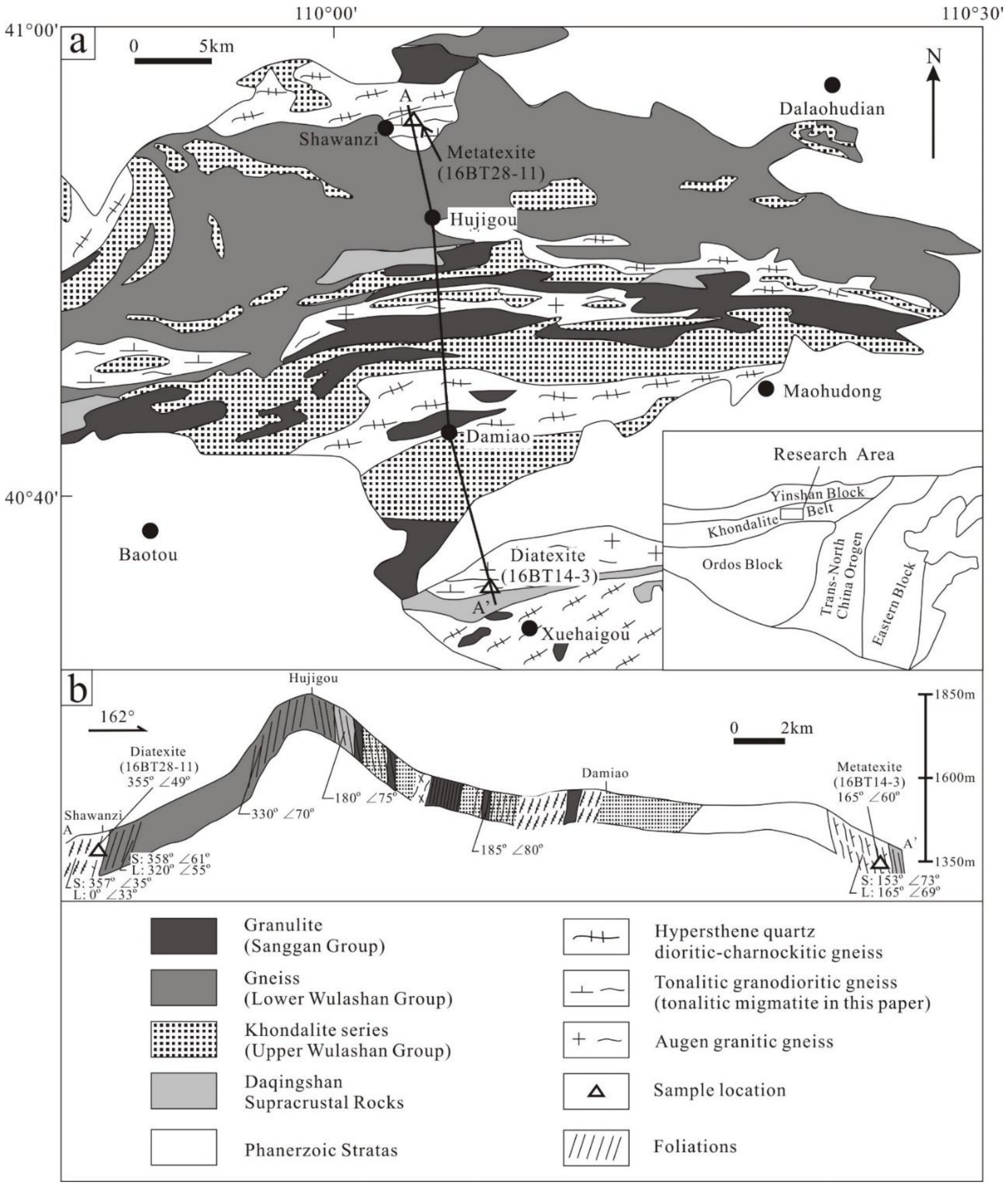

Figure 1. Geological map (a) with a simplified cross-section along A-A' (b) in the Daqingshan area, inset reveals the location in North China Craton (NCC), modified from Zhao et al. (2005), Xu et al. (2007) and Wan et al. (2013). Numbers refer to selected samples' azimuth and dip of foliation (S)/lineation (L). Samples' localities are also marked.

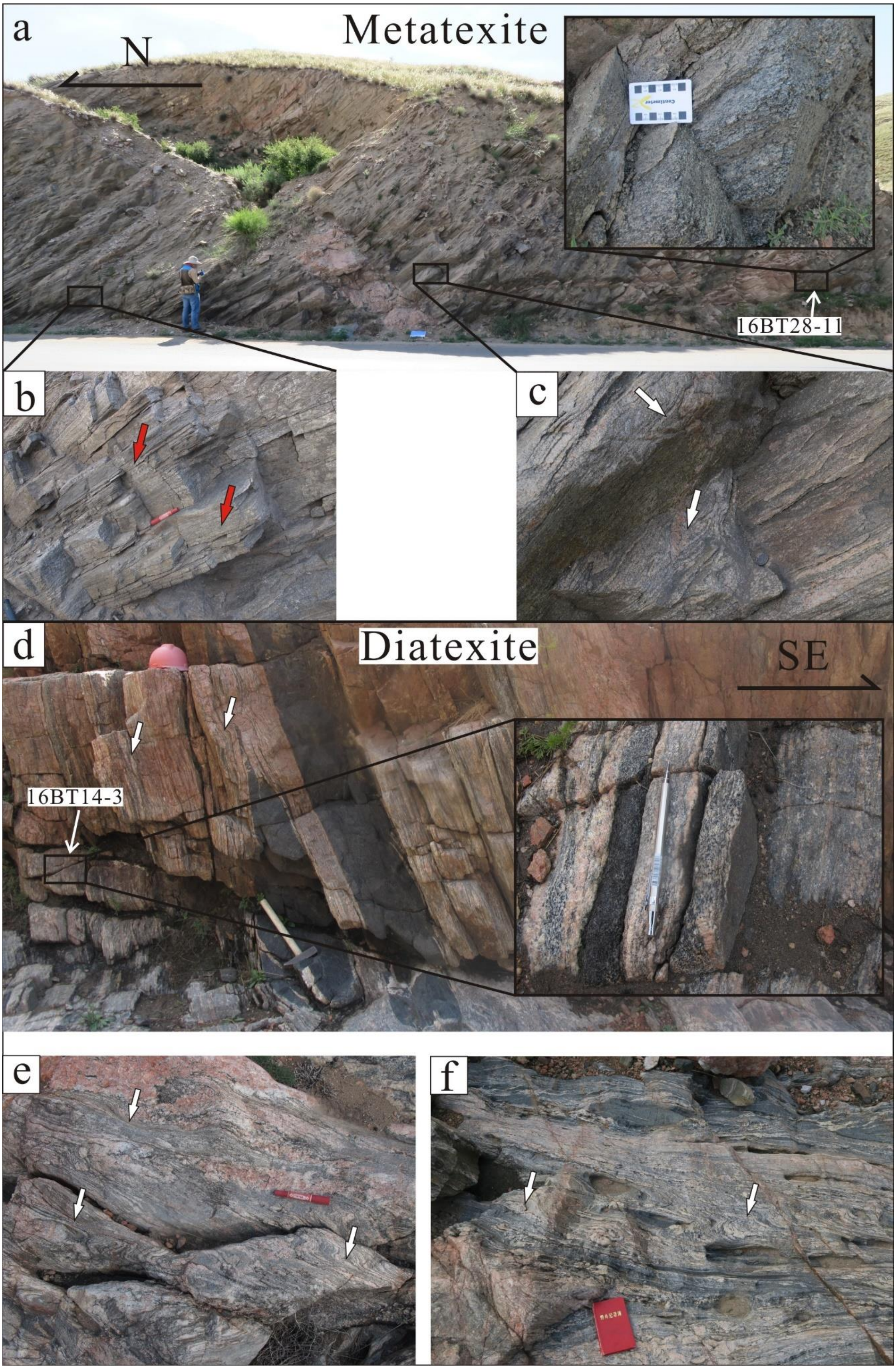

1104
1105

Figure 2. Outcrop characteristics of tonalitic migmatite sampled in northern (metatexite, a-c) and southern research area (diatexite, d-f); (a) profile near Shawanzi; (b) banded layers; (c) stromatic to net layers; (d) profile near Xuehaigou with syn-tectonic characters; (e) and (f) are outcrops with numerous anatectic structures. Red arrows: band features; white arrows: flow features.

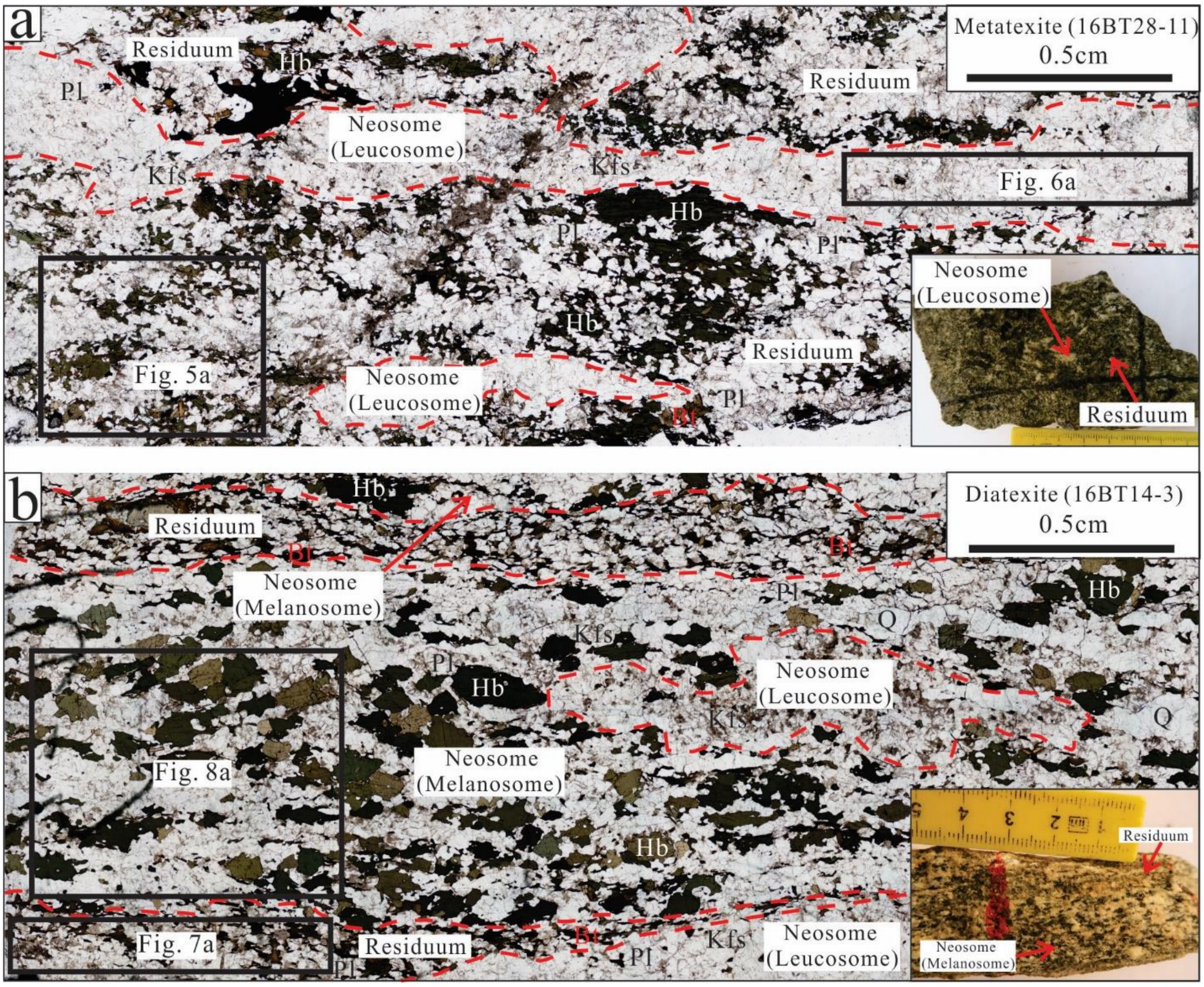

Figure 3. Oriented thin section microphotographs (plane-polarized light) of tonalitic migmatites; (a) metatexite and (b) diatexite; residuum and neosome (leucosome or melanosome) domains are labelled and boundaries shown as red dashed lines; insets show the respective hand specimen and representative domains' locations; black rectangles show location of the EBSD map areas.

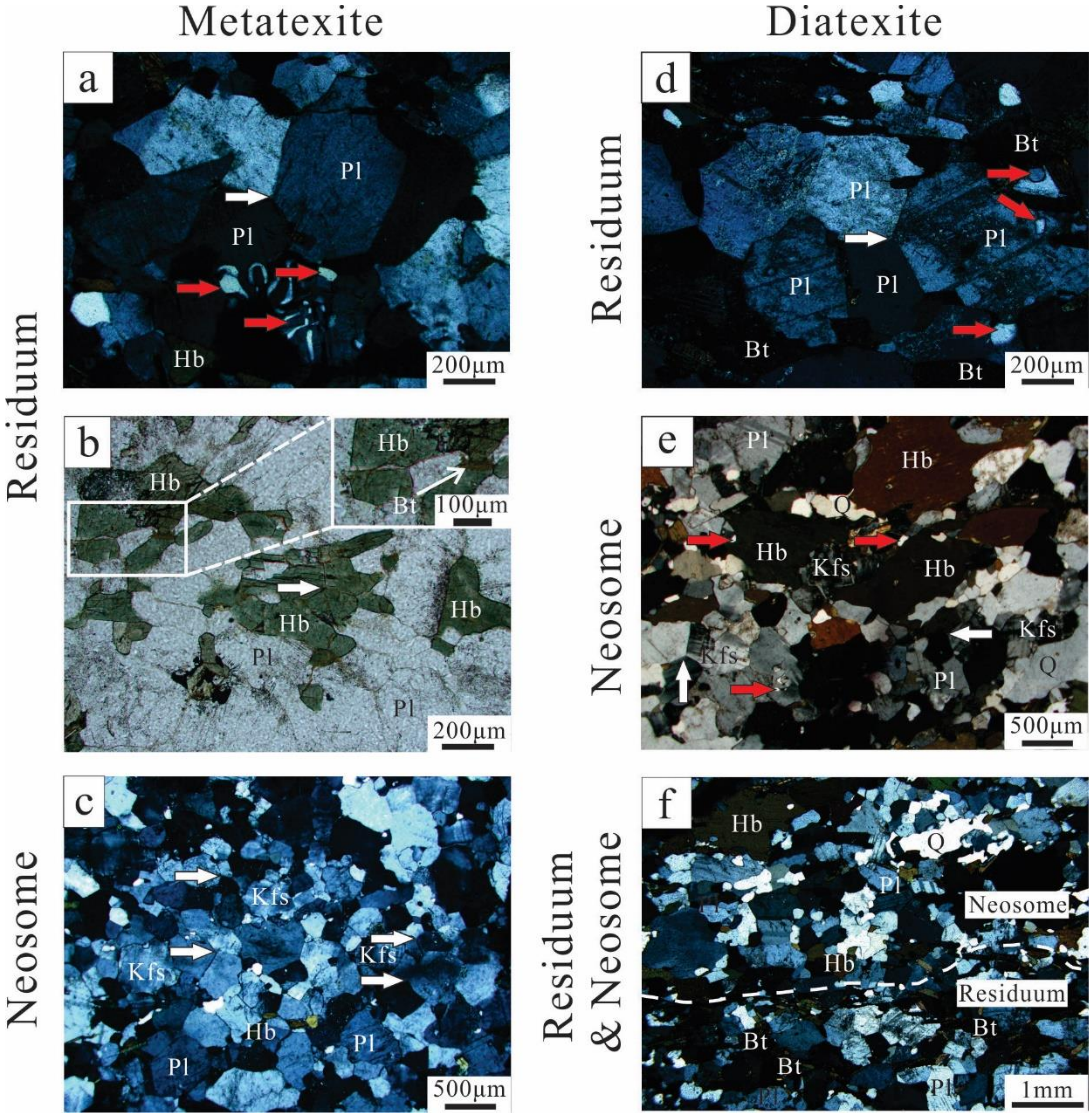

Figure 4. Photomicrographs of general microstructures of (a-c) metatexite and (d-f) diatexite. All the photos are cross-polarized light except for (b), which shows plane light; (a) residuum: equilibrium triple-junction (white arrow), K-feldspar inclusions and myrmekite textures (red arrows) between plagioclase grains, (b) residuum: anhedral hornblende grains with straight to concave grain boundaries, overprinted by ~120° triple-junction (white arrow), inset shows that biotite is surrounded by hornblende (c) neosome: mixture of even-grained plagioclase and K-feldspar with numerous equilibrium triple-junctions (white arrows), (d) residuum: plagioclase grains with straight boundaries, quartz inclusions (red arrows) and equilibrium triple junctions (white arrows), (e) neosome: 120° triple junctions exist between feldspar grains (white arrows), K-feldspar aggregates within a matrix of hornblende (coarser grained), plagioclase, quartz inclusions and myrmekite (red arrows), (f) boundary of residuum (biotite dominant) and neosome (hornblende dominant).

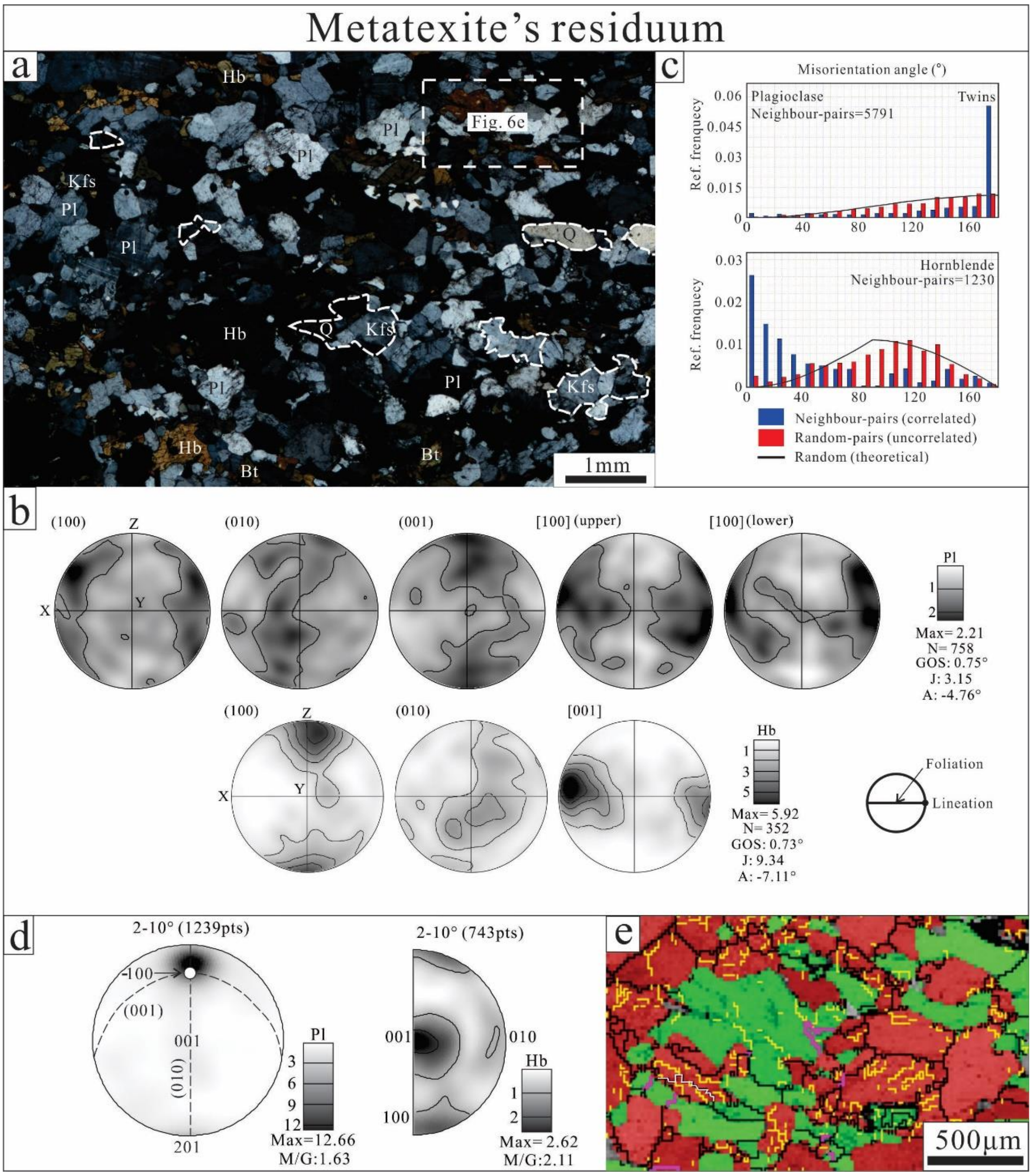

Figure 5. Orientation characteristics and EBSD map of metatexite's residuum : (a) typical microstructure and EBSD data area in microphotograph (cross-polars); (b) crystal orientation of plagioclase and hornblende, with foliation and lineation shown; X – lineation, XY - foliation; (c) MAD for plagioclase and hornblende; (d) misorientation axes distribution of subgrain boundaries for plagioclase and hornblende, note the strong maxima for plagioclase around the [-100] axis; (e) representative EBSD map in residuum. White dashed line: K-feldspar and/or quartz dominant aggregate; Max: maximum density; N: number of valid mineral grains; J: J-index; A: average angle between valid grain's long axis and foliation direction (or horizontal); M/G: MXD axes/grain amounts ratio; black line: grain boundary (>10°); yellow and purple lines signify subgrain boundaries between 2~5° and 5~10°, respectively; white line: twin boundary. Grey areas are not indexed.

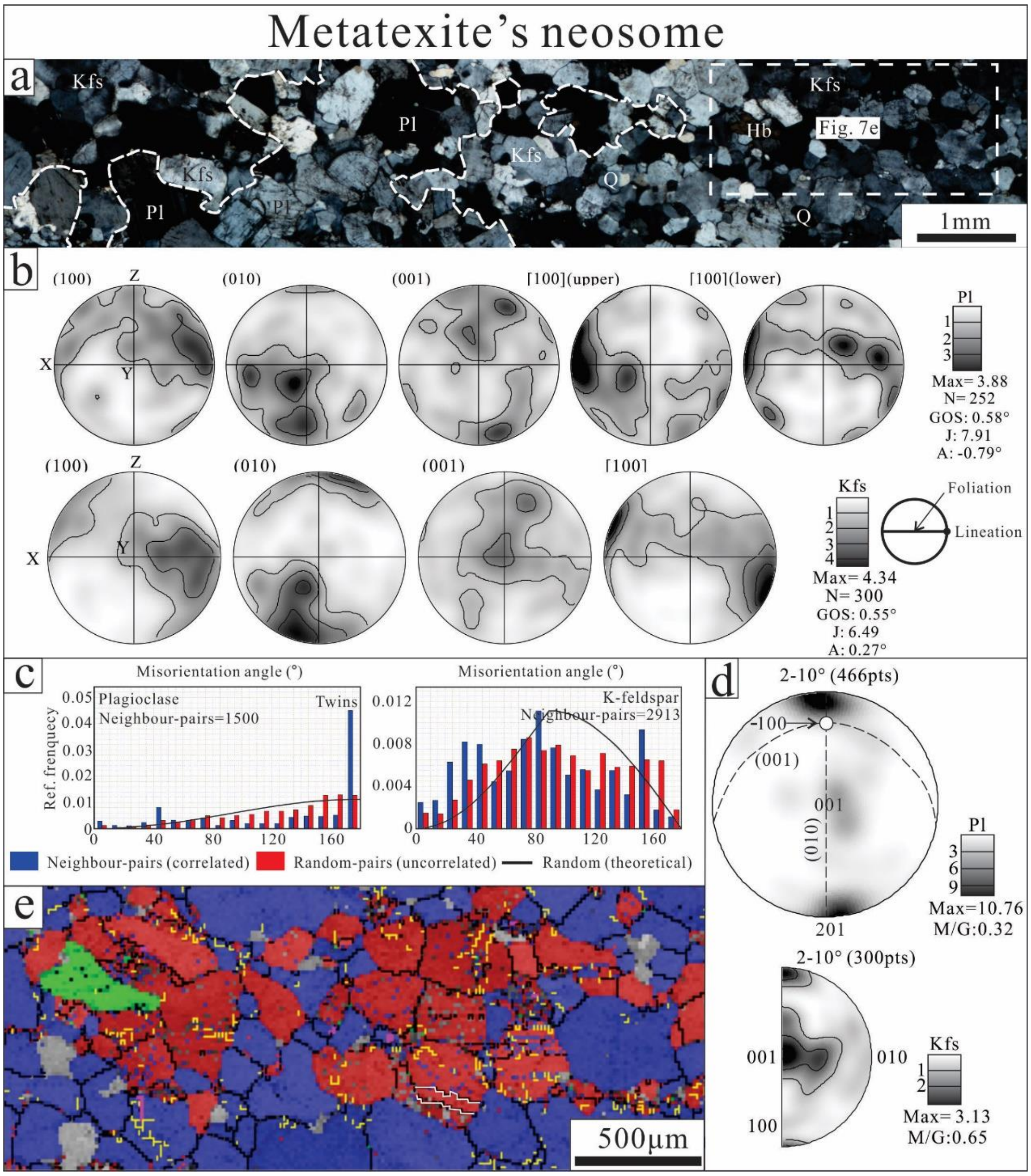

Figure 6. Orientation characteristics and EBSD map of metatexite's neosome: (a) typical microstructure and EBSD data area in microphotograph (cross-polars); (b) crystal orientation of plagioclase and K-feldspar, with foliation and lineation shown; X – lineation, XY - foliation; (c) MAD for plagioclase and K-feldspar; (d) misorientation axes distribution for plagioclase and K-feldspar; (e) representative EBSD map in leucosome. White dashed line: plagioclase dominant aggregates (sometimes with hornblende). Blue: K-feldspar; Red: plagioclase; Green: hornblende; other parameters and legends are same as shown in Figure 5.

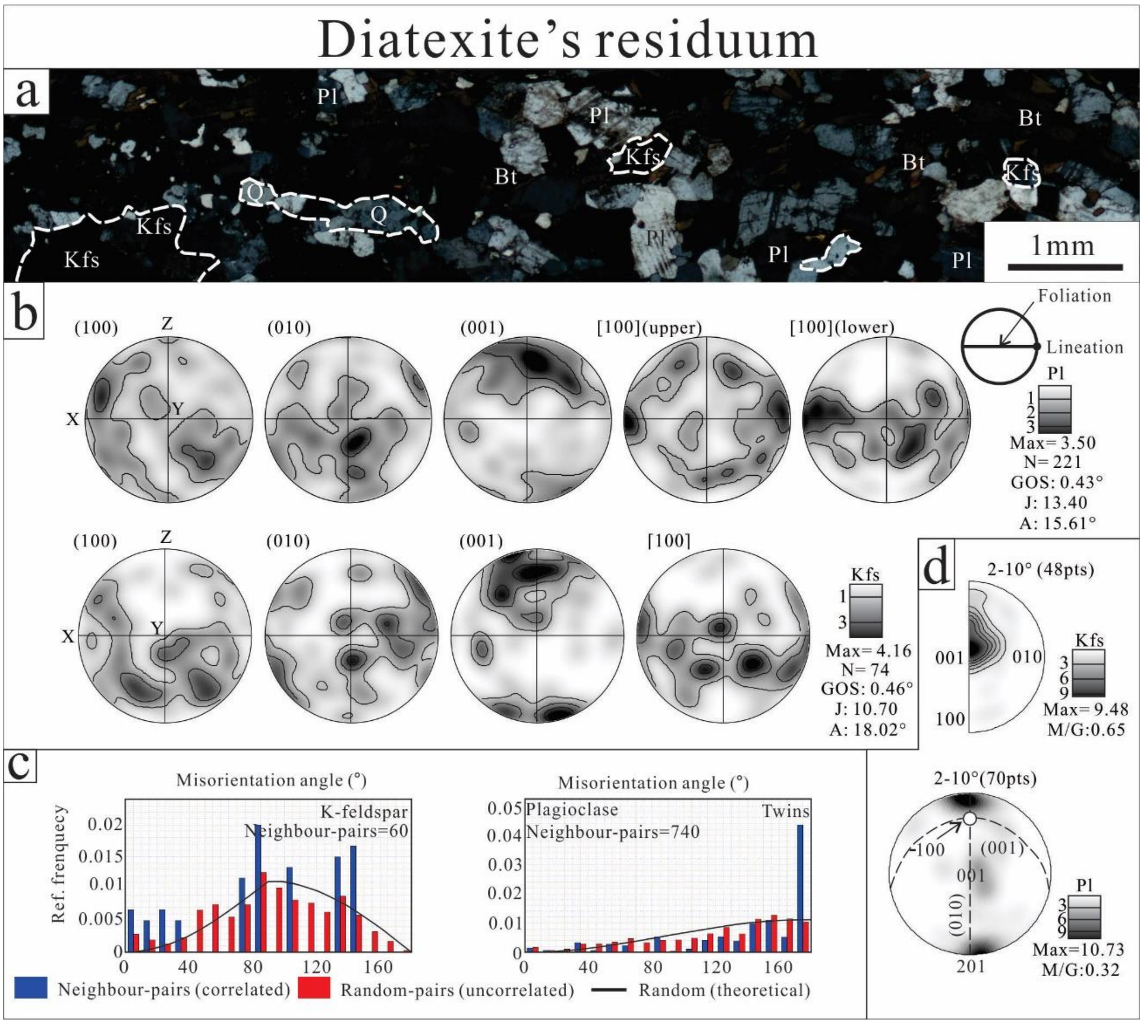

Figure 7. Orientation characteristics of diatexite's residuum: (a) typical microstructure and EBSD data area in microphotograph (cross-polars); (b) crystal orientation of plagioclase and K-feldspar, with foliation and lineation shown; X – lineation, XY - foliation; ; (c) MAD for plagioclase and K-feldspar; (d) misorientation axes distribution for plagioclase and K-feldspar. All the parameters and legends are the same as Figure 5 shows.

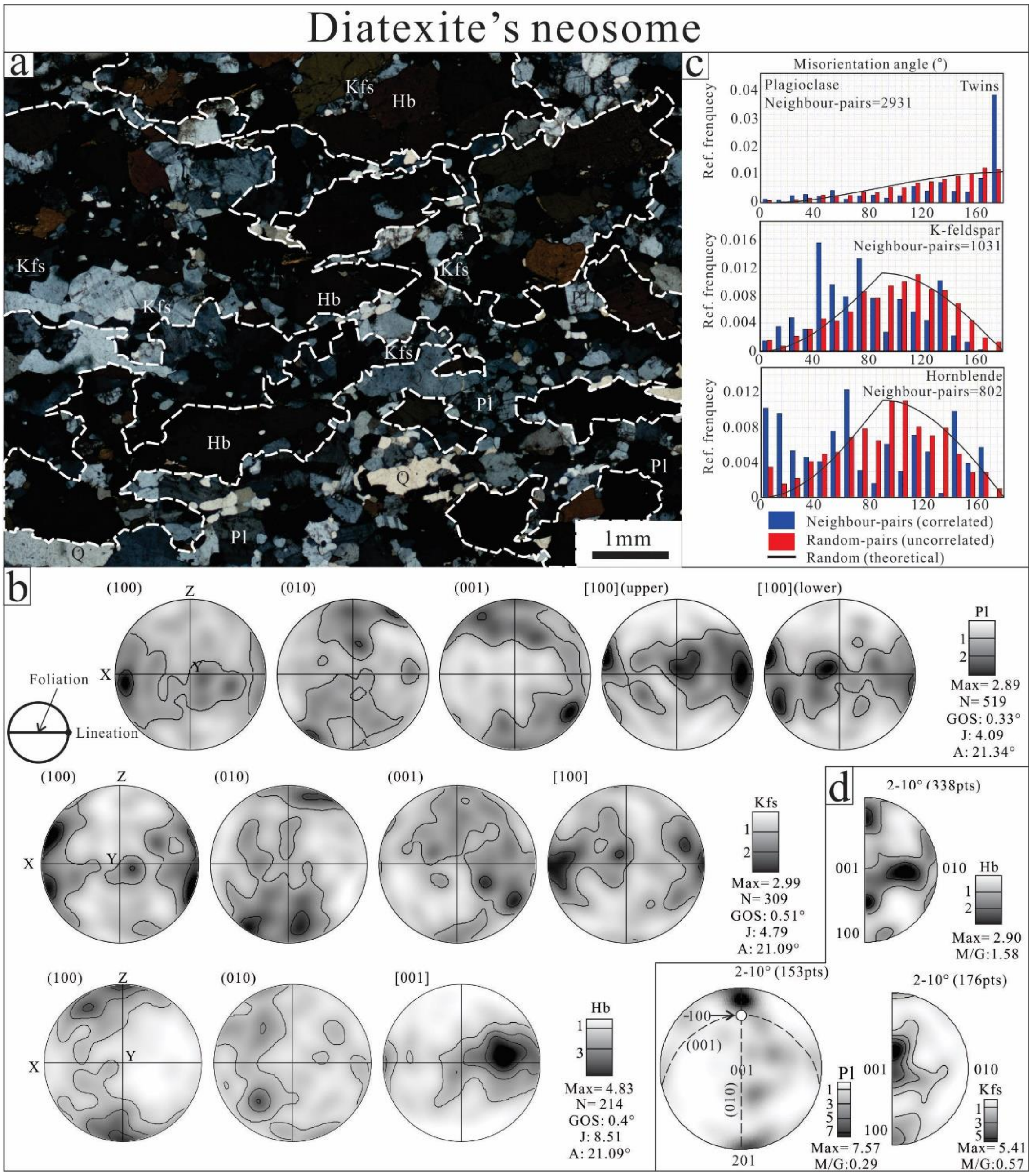

Figure 8. Orientation characteristics of diatexite's neosome: (a) typical microstructure and EBSD data area in microphotograph (cross-polars); (b) crystal orientation of plagioclase, K-feldspar and hornblende, with foliation and lineation shown; X – lineation, XY - foliation; ; (c) MAD for plagioclase, K-feldspar and hornblende; (d) misorientation axes distribution for plagioclase, K-feldspar and hornblende. White dashed line: represent plagioclase and hornblende dominant aggregates. All the parameters and legends are the same as Figure 5 shows.

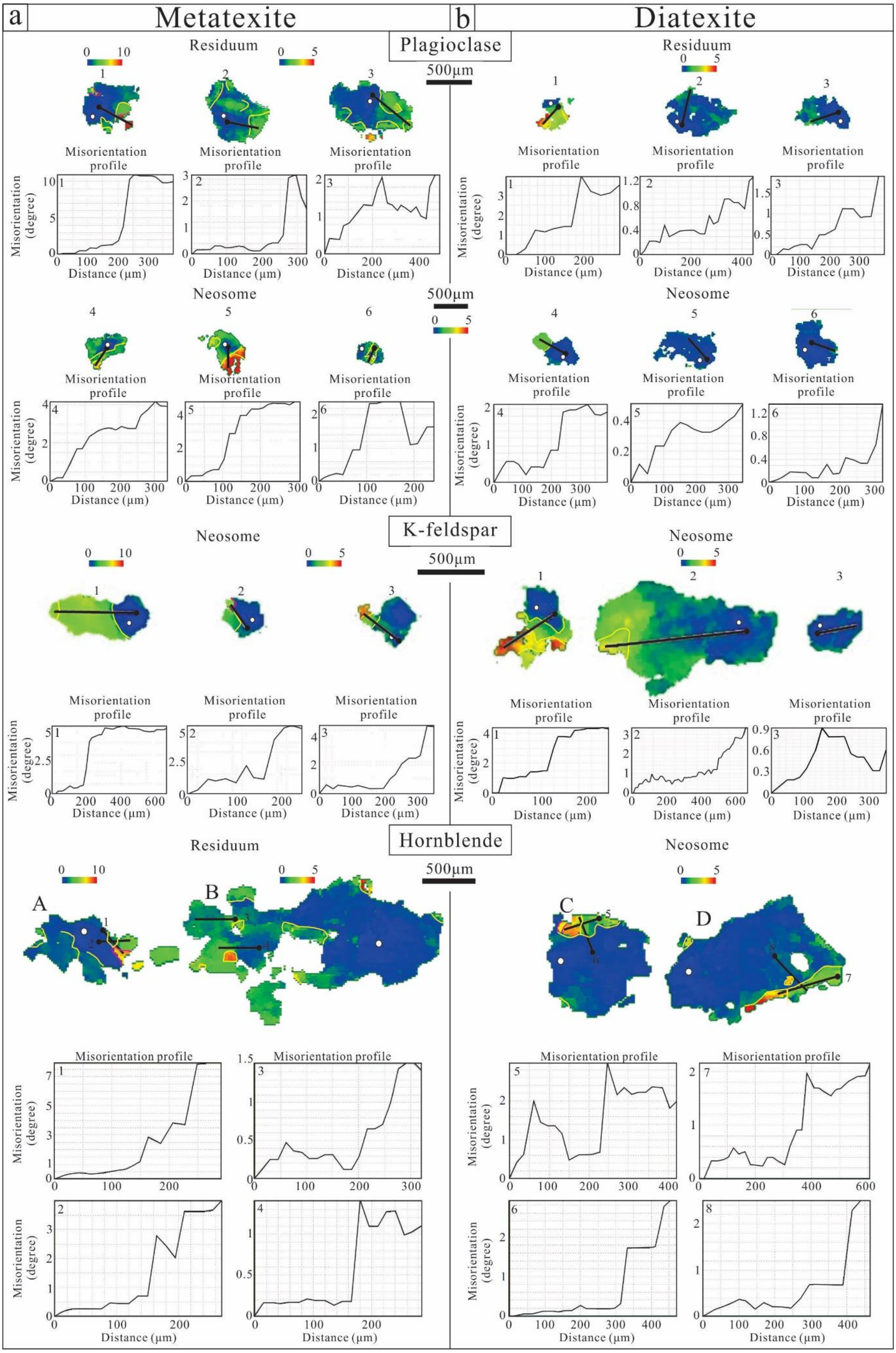

a
Metatexite
b
Diatexite
Plagioclase
Residuum
Neosome
K-feldspar
Hornblende
500μm
Misorientation profile
Misorientation (degree)
Distance (μm)
A
B
C
D

Figure 9. Typical intracrystalline deformation features of plagioclase, K-feldspar and hornblende grains in metatexite (a) and diatexite (b). Orientation changes are shown in degrees relative to a reference orientation (marked as white spot); the starting point for misorientation profiles are shown (0 μm) is marked as black spot; yellow and purple lines represent 2-5° and 5-10° subgrain boundaries.

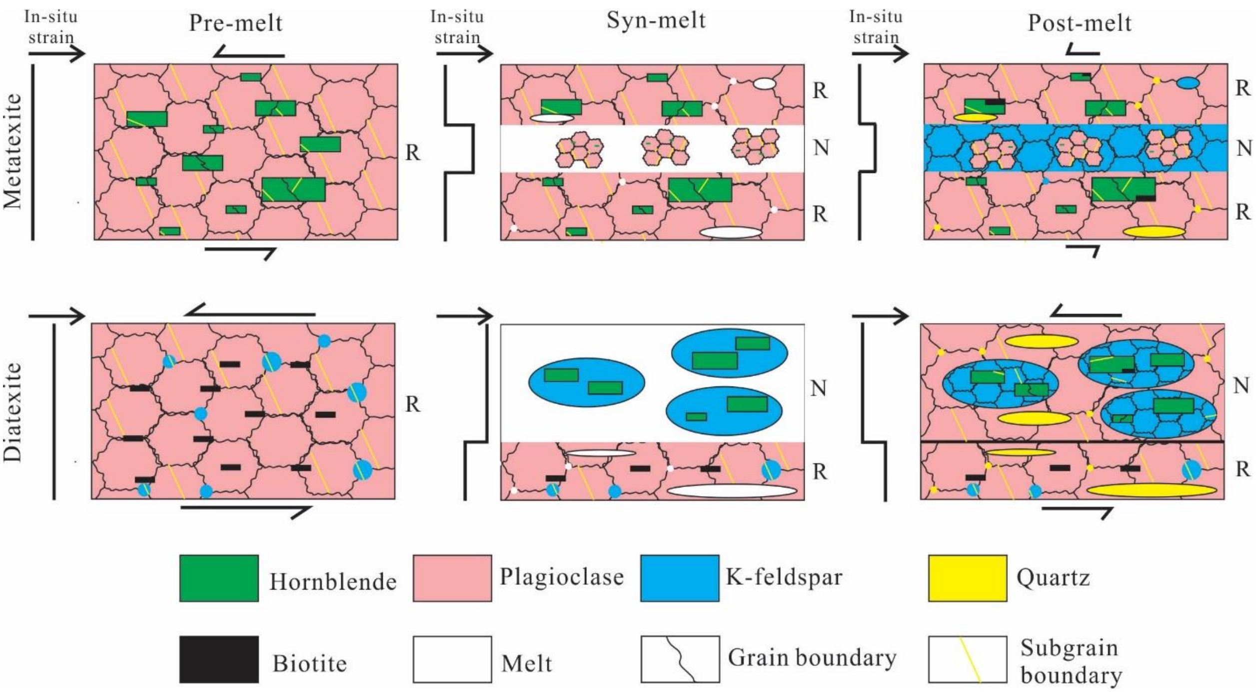

Figure 10. Models of migmatites' deformational evolution procedures in pre-, syn-, and post-melt stages in ductile shearing environment (not to scale). The arrow represents strain increasing and the fold line represent relative strain degree in different domains. R: residuum; N: neosome.

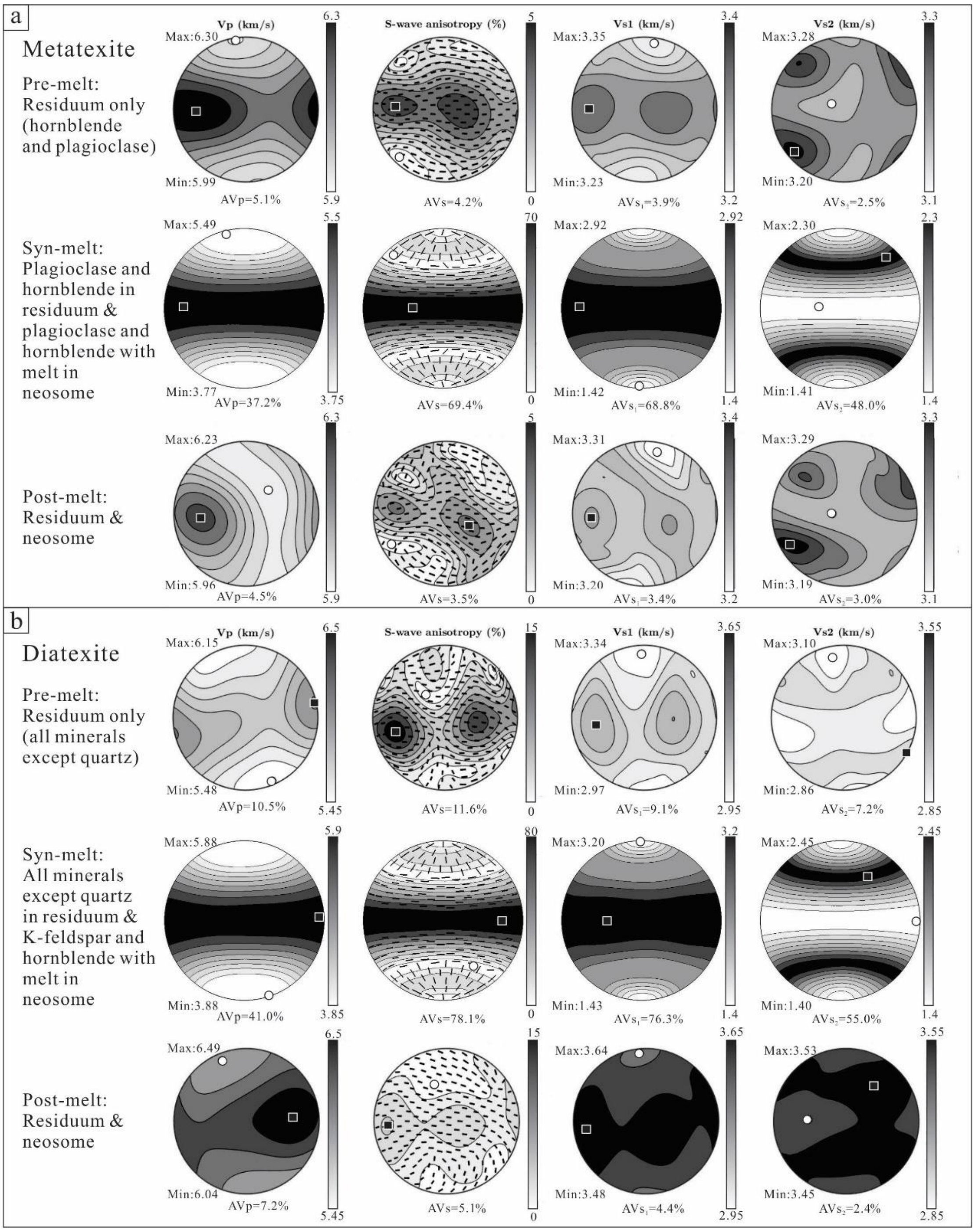

Figure 11. Seismic properties in pre-melt, syn-melt and post-melt conditions of metatexite (a) and diatexite (b) in Daqingshan area. From left to right are 3-D distributions of P-wave velocities (Vp), S-wave anisotropy with orientations of fast shear wave polarization plane, fast and slow S-wave velocities (Vs_1 and Vs_2), separately. Black square: maximum value; white circle: minimum value. Scale migmatite's pre- and post-melt conditions are accordant. AVp: maximum Vp anisotropy; AVs: maximum Vs anisotropy; AVs_1: maximum Vs_1 anisotropy; AVs_2: maximum Vs_2 anisotropy.

Figure1.

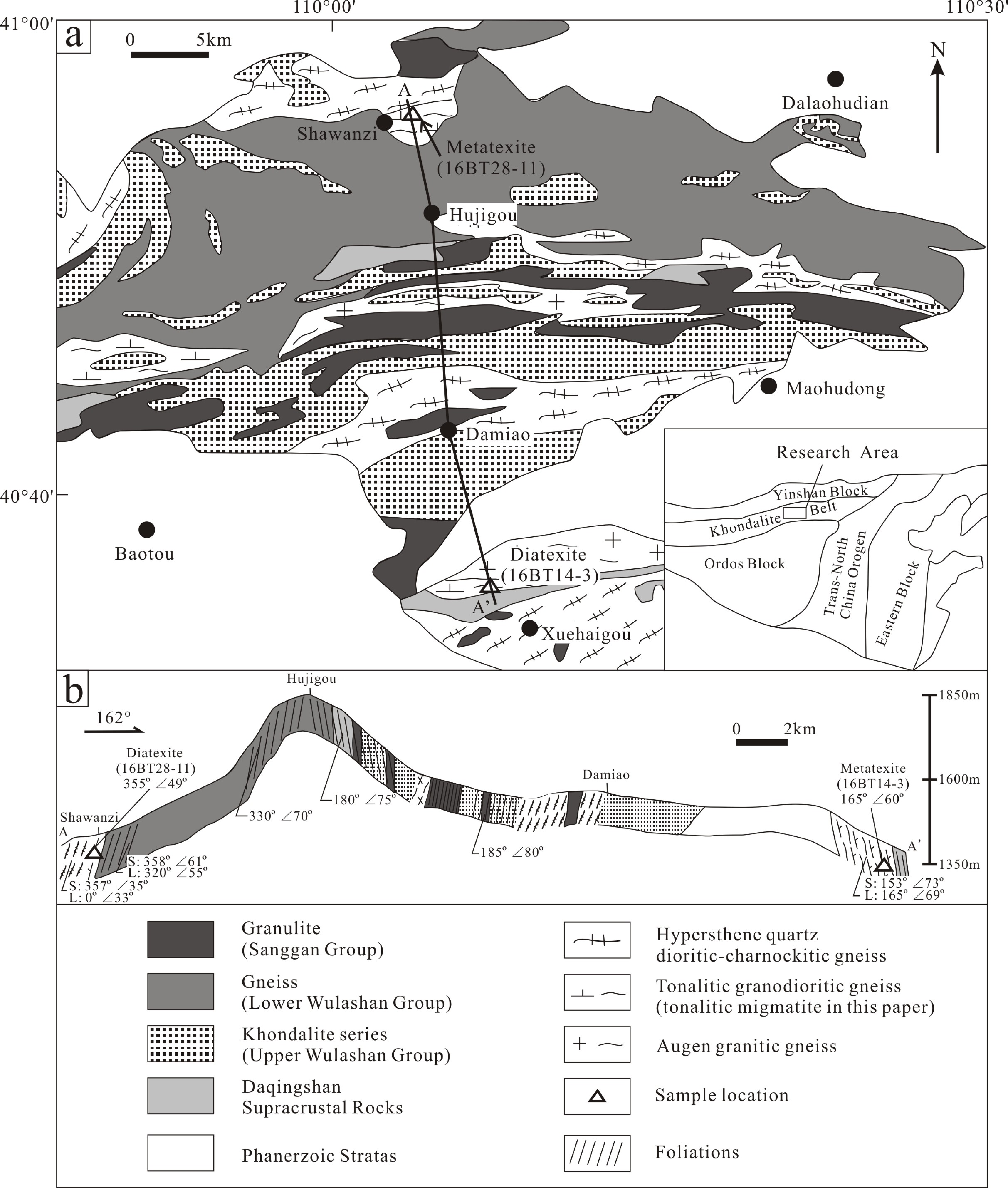
110°00'
110°30'
41°00'
40°40'
a
0
5km
N
A
Shawanzi
Metatexite
(16BT28-11)
Dalaohudian
Hujigou
Maohudong
Damiao
Baotou
Diatexite
(16BT14-3)
A'
Xuehaigou
Research Area
Yinshan Block
Khondalite
Belt
Ordos Block
Trans-North
China Orogen
Eastern Block
b
Hujigou
162°
Diatexite
(16BT28-11)
355° ∠49°
Shawanzi
A
S: 358° ∠61°
L: 320° ∠55°
S: 357° ∠35°
L: 0° ∠33°
330° ∠70°
180° ∠75°
185° ∠80°
Damiao
0
2km
Metatexite
(16BT14-3)
165° ∠60°
A'
S: 153° ∠73°
L: 165° ∠69°
1850m
1600m
1350m
Granulite
(Sanggan Group)
Gneiss
(Lower Wulashan Group)
Khondalite series
(Upper Wulashan Group)
Daqingshan
Supracrustal Rocks
Phanerzoic Stratas
Hypersthene quartz
dioritic-charnockitic gneiss
Tonalitic granodioritic gneiss
(tonalitic migmatite in this paper)
Augen granitic gneiss
Sample location
Foliations

Figure2.


a
Metatexite
N
16BT28-11
b
c
d
Diatexite
SE
16BT14-3
e
f

Figure3.

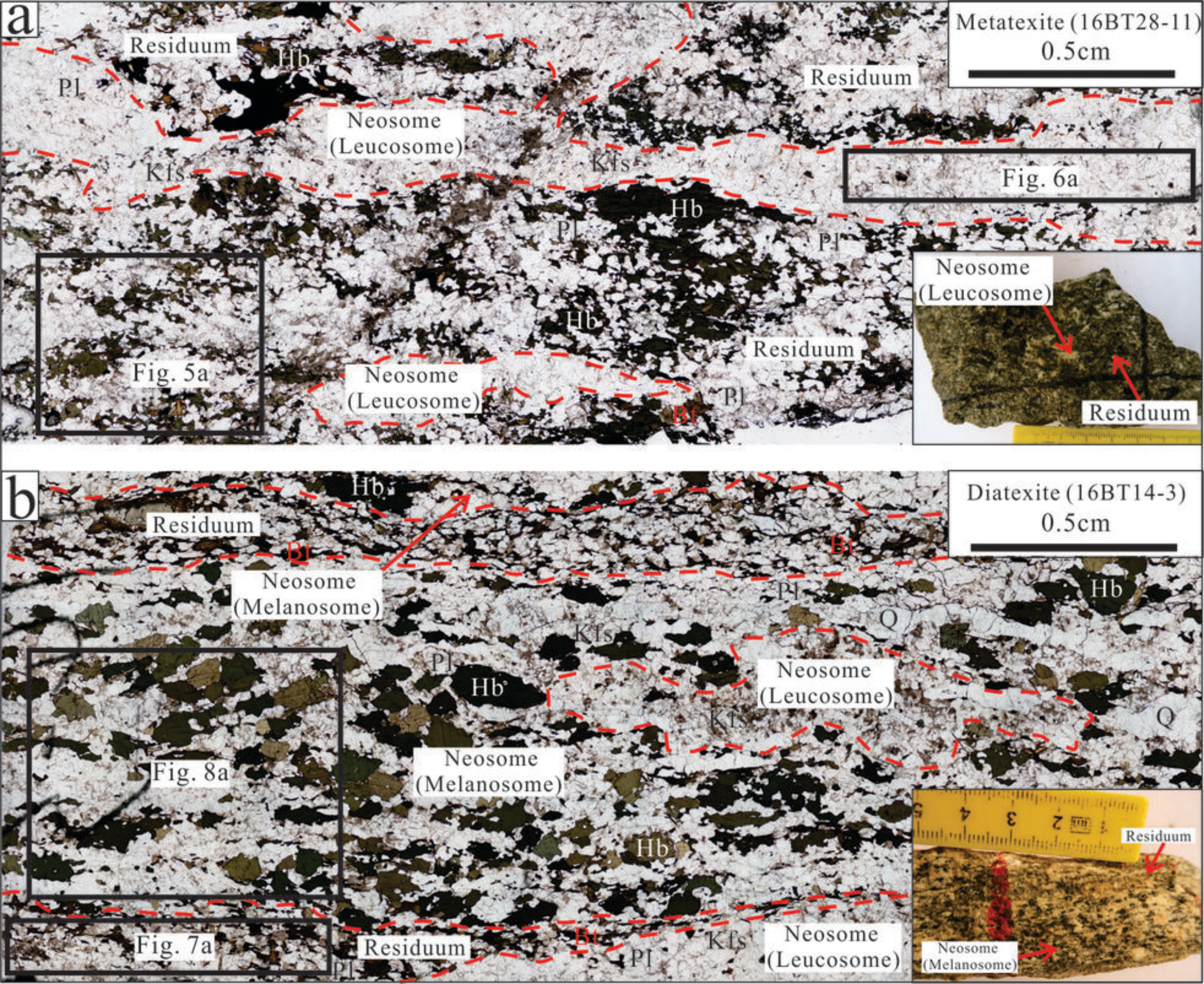
a
Metatexite (16BT28-11)
0.5cm
Residuum
Hb
Pl
Neosome
(Leucosome)
Kfs
Residuum
Fig. 6a
Hb
Pl
Pl
Hb
Residuum
Fig. 5a
Neosome
(Leucosome)
Bt
Pl
Neosome
(Leucosome)
Residuum
b
Diatexite (16BT14-3)
0.5cm
Hb
Residuum
Bt
Neosome
(Melanosome)
Bt
Pl
Hb
Q
Kfs
Pl
Hb
Neosome
(Leucosome)
Kfs
Q
Fig. 8a
Neosome
(Melanosome)
Hb
Fig. 7a
Residuum
Bt
Pl
Kfs
Neosome
(Leucosome)
Pl
Residuum
Neosome
(Melanosome)

Figure4.

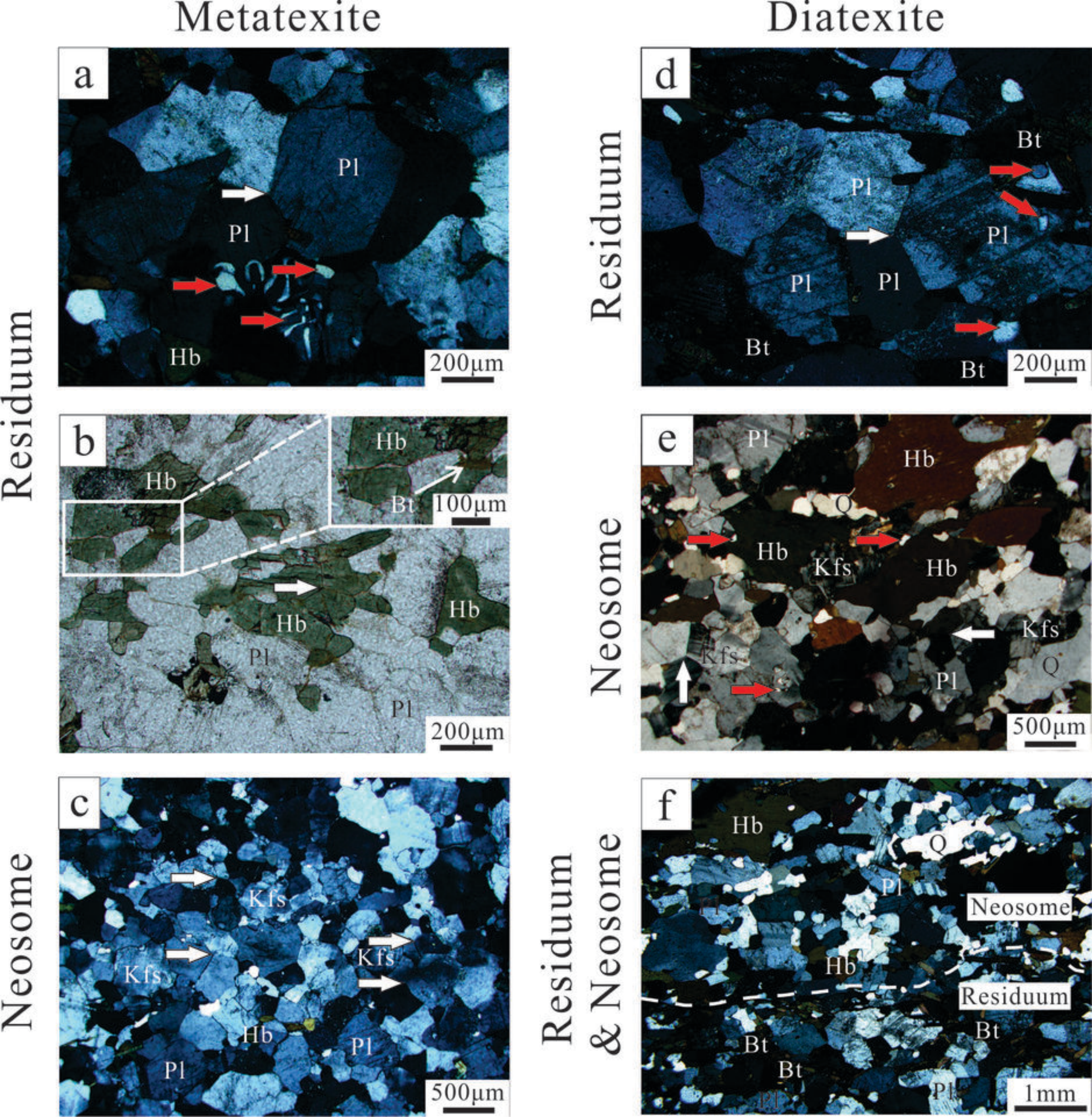

Metatexite
Diatexite
Residuum
Neosome
Residuum
Neosome
Residuum & Neosome
a
Pl
Pl
Hb
200μm
b
Hb
Hb
Bt
100μm
Hb
Hb
Pl
Pl
200μm
c
Kfs
Kfs
Kfs
Hb
Pl
Pl
Pl
500μm
d
Bt
Pl
Pl
Pl
Pl
Bt
Bt
200μm
e
Pl
Hb
Q
Hb
Kfs
Hb
Kfs
Kfs
Q
Pl
500μm
f
Hb
Q
Pl
Pl
Neosome
Hb
Residuum
Bt
Bt
Bt
Pl
Pl
1mm

Figure5.

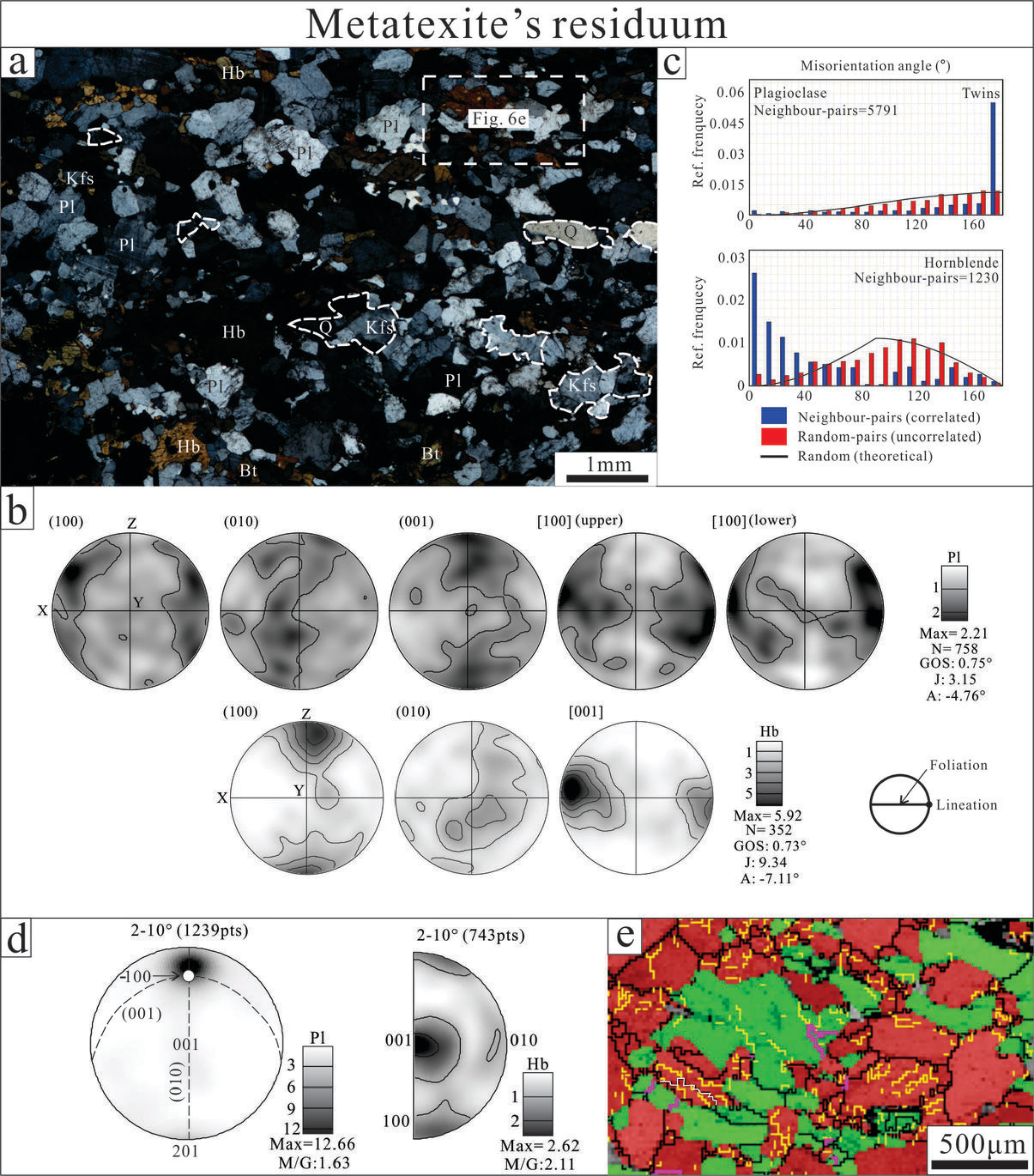
Metatexite's residuum
a
Hb
Fig. 6e
Pl
Kfs
Q
Bt
1mm
c
Misorientation angle (°)
Plagioclase
Neighbour-pairs=5791
Twins
Ref. frenquecy
Hornblende
Neighbour-pairs=1230
Neighbour-pairs (correlated)
Random-pairs (uncorrelated)
Random (theoretical)
b
(100)
(010)
(001)
[100] (upper)
[100] (lower)
Z
X
Y
Pl
Max= 2.21
N= 758
GOS: 0.75°
J: 3.15
A: -4.76°
[001]
Hb
Max= 5.92
N= 352
GOS: 0.73°
J: 9.34
A: -7.11°
Foliation
Lineation
d
2-10° (1239pts)
-100
(001)
001
(010)
201
Max=12.66
M/G:1.63
2-10° (743pts)
001
010
100
Max= 2.62
M/G:2.11
e
500μm

Figure6.

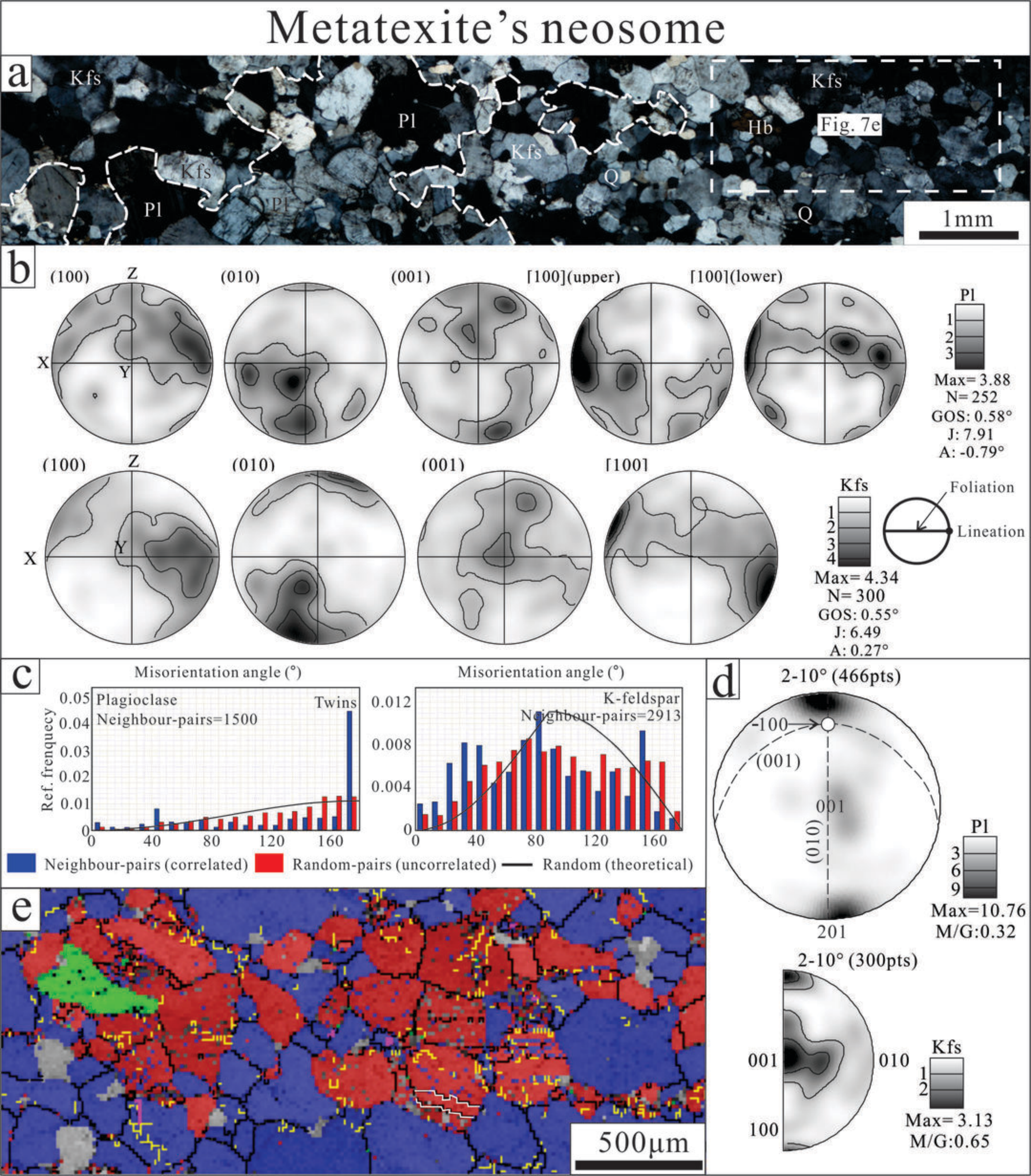
Metatexite's neosome
a
Kfs
Pl
Kfs
Pl
Pl
Kfs
Q
Hb
Fig. 7e
Kfs
Q
1mm
b
(100)
Z
X
Y
(010)
(001)
[100](upper)
[100](lower)
Pl
1
2
3
Max= 3.88
N= 252
GOS: 0.58°
J: 7.91
A: -0.79°
(100)
Z
X
Y
(010)
(001)
[100]
Kfs
1
2
3
4
Foliation
Lineation
Max= 4.34
N= 300
GOS: 0.55°
J: 6.49
A: 0.27°
c
Misorientation angle (°)
Plagioclase
Neighbour-pairs=1500
Twins
Ref. frenquecy
0.05
0.04
0.03
0.02
0.01
0
0
40
80
120
160
Misorientation angle (°)
K-feldspar
Neighbour-pairs=2913
0.012
0.008
0.004
0
0
40
80
120
160
Neighbour-pairs (correlated)
Random-pairs (uncorrelated)
Random (theoretical)
d
2-10° (466pts)
-100
(001)
001
(010)
201
Pl
3
6
9
Max=10.76
M/G:0.32
2-10° (300pts)
001
010
100
Kfs
1
2
Max= 3.13
M/G:0.65
e
500μm

Figure7.

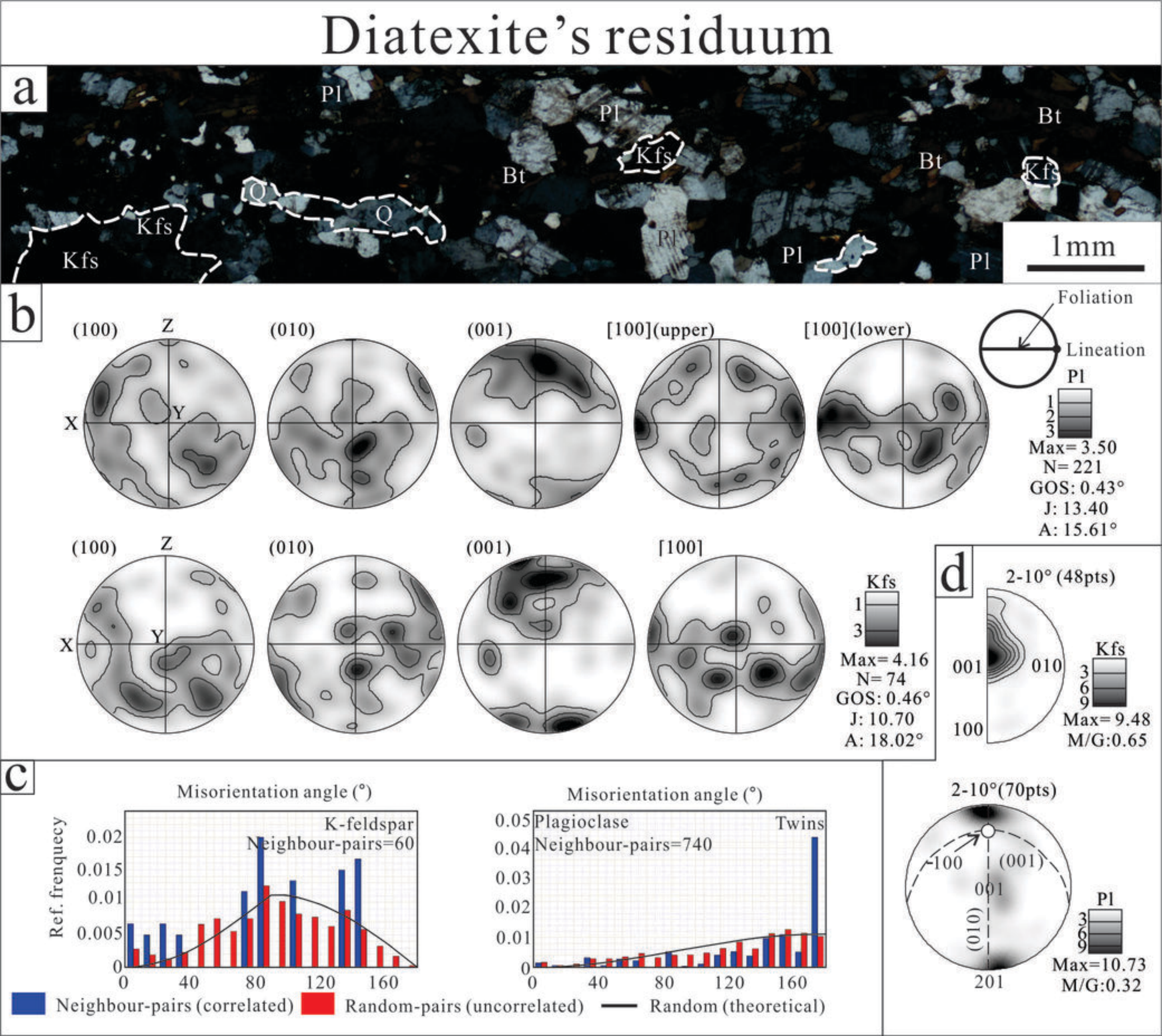

Diatexite's residuum
a
Pl
Pl
Kfs
Bt
Bt
Bt
Kfs
Q
Q
Kfs
Kfs
Pl
Pl
Pl
1mm
b
(100)
Z
X
Y
(010)
(001)
[100](upper)
[100](lower)
Foliation
Lineation
Pl
1
2
3
Max= 3.50
N= 221
GOS: 0.43°
J: 13.40
A: 15.61°
(100)
Z
X
Y
(010)
(001)
[100]
Kfs
1
3
Max= 4.16
N= 74
GOS: 0.46°
J: 10.70
A: 18.02°
d
2-10° (48pts)
001
010
100
Kfs
3
6
9
Max= 9.48
M/G:0.65
c
Misorientation angle (°)
Ref. frenquecy
K-feldspar
Neighbour-pairs=60
Misorientation angle (°)
Plagioclase
Neighbour-pairs=740
Twins
Neighbour-pairs (correlated)
Random-pairs (uncorrelated)
Random (theoretical)
2-10°(70pts)
-100
(001)
001
(010)
201
Pl
3
6
9
Max=10.73
M/G:0.32

Figure8.

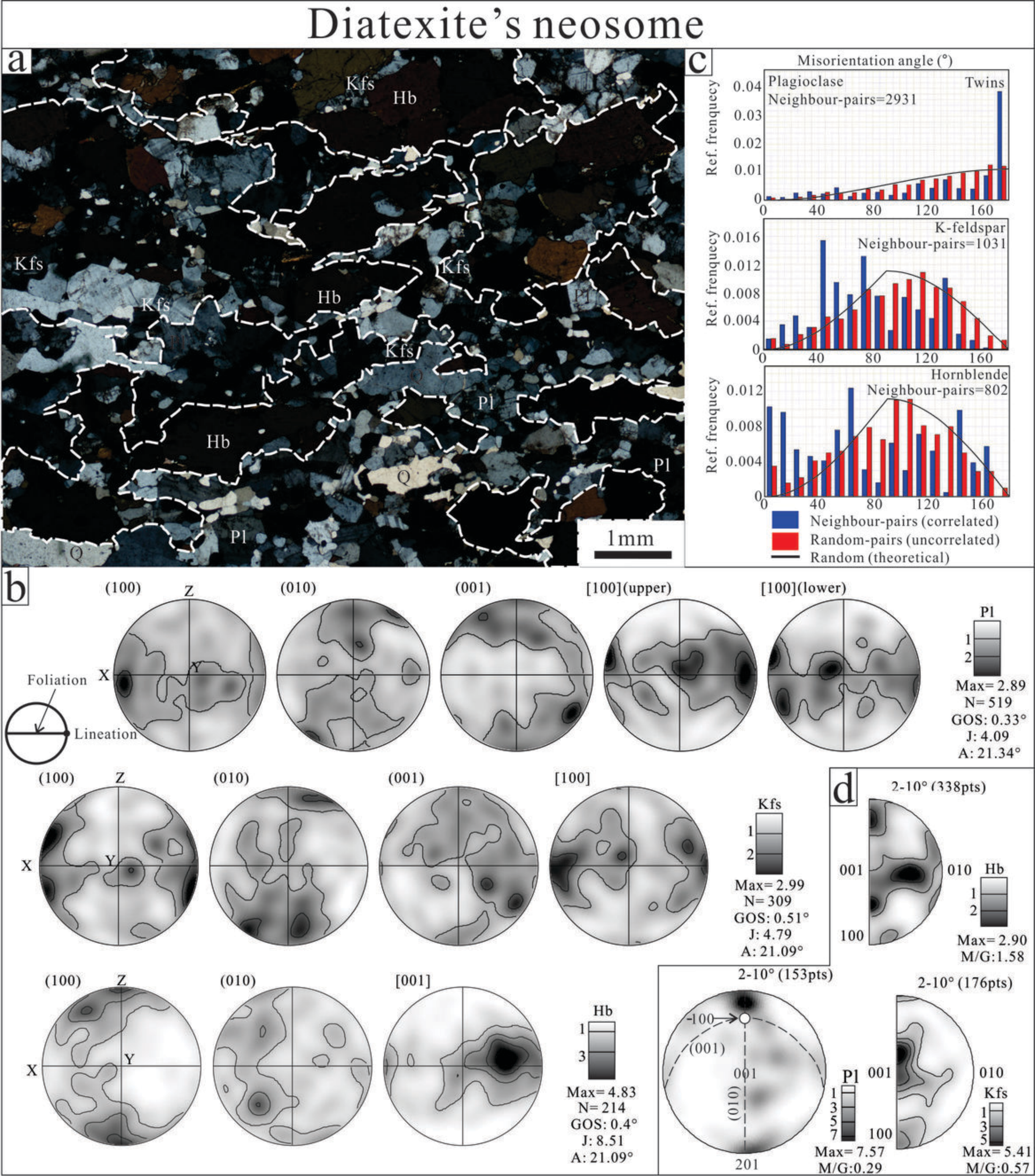
Diatexite's neosome
a
Kfs
Hb
Kfs
Kfs
Hb
Kfs
Pl
Kfs
Pl
Hb
Q
Pl
Pl
Q
1mm
c
Misorientation angle (°)
Plagioclase
Neighbour-pairs=2931
Twins
Ref. frenquecy
K-feldspar
Neighbour-pairs=1031
Hornblende
Neighbour-pairs=802
Neighbour-pairs (correlated)
Random-pairs (uncorrelated)
Random (theoretical)
b
(100)
(010)
(001)
[100](upper)
[100](lower)
Foliation
Lineation
Z
X
Y
Pl
Max= 2.89
N= 519
GOS: 0.33°
J: 4.09
A: 21.34°
[100]
Kfs
Max= 2.99
N= 309
GOS: 0.51°
J: 4.79
A: 21.09°
[001]
Hb
Max= 4.83
N= 214
GOS: 0.4°
J: 8.51
A: 21.09°
d
2-10° (338pts)
001
010
100
Hb
Max= 2.90
M/G:1.58
2-10° (153pts)
-100
(001)
001
(010)
201
Pl
Max= 7.57
M/G:0.29
2-10° (176pts)
001
010
100
Kfs
Max= 5.41
M/G:0.57

Figure9.

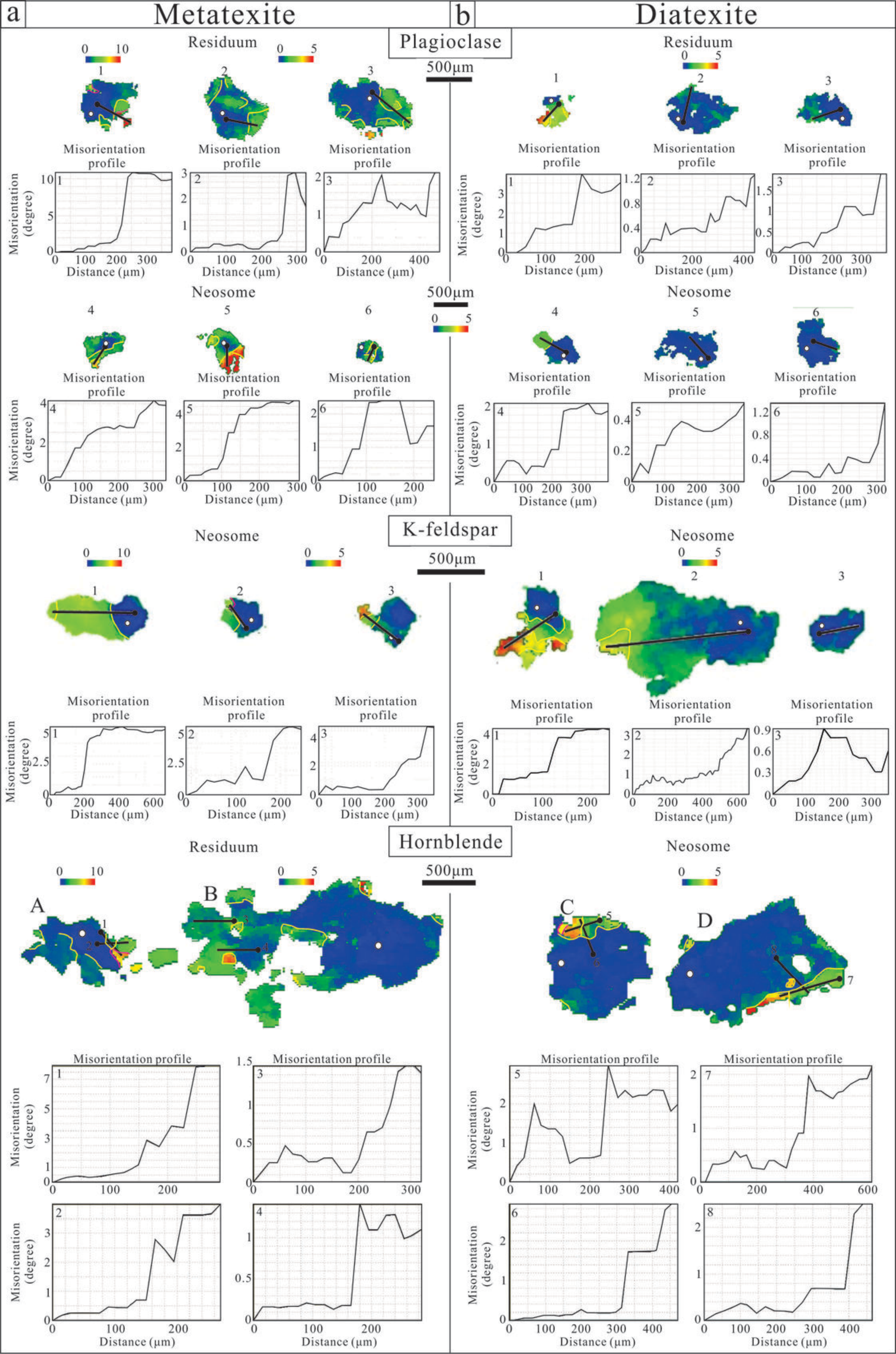

a
Metatexite
b
Diatexite
Plagioclase
Residuum
Neosome
K-feldspar
Hornblende
500μm
Misorientation profile
Misorientation (degree)
Distance (μm)
A
B
C
D

Figure10.

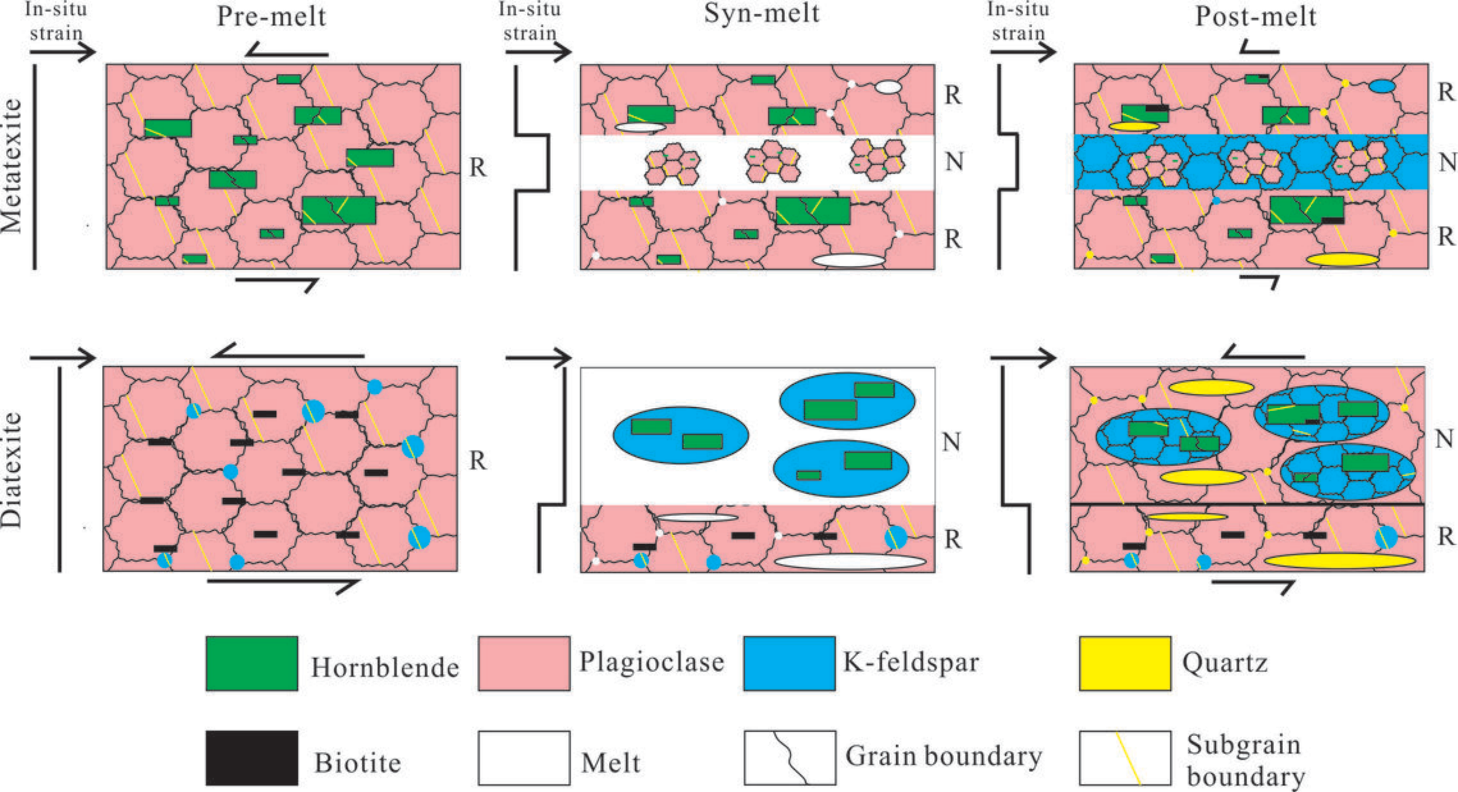

In-situ strain
Pre-melt
In-situ strain
Syn-melt
In-situ strain
Post-melt
Metatexite
Diatexite
R
N
Hornblende
Plagioclase
K-feldspar
Quartz
Biotite
Melt
Grain boundary
Subgrain boundary

Figure11.

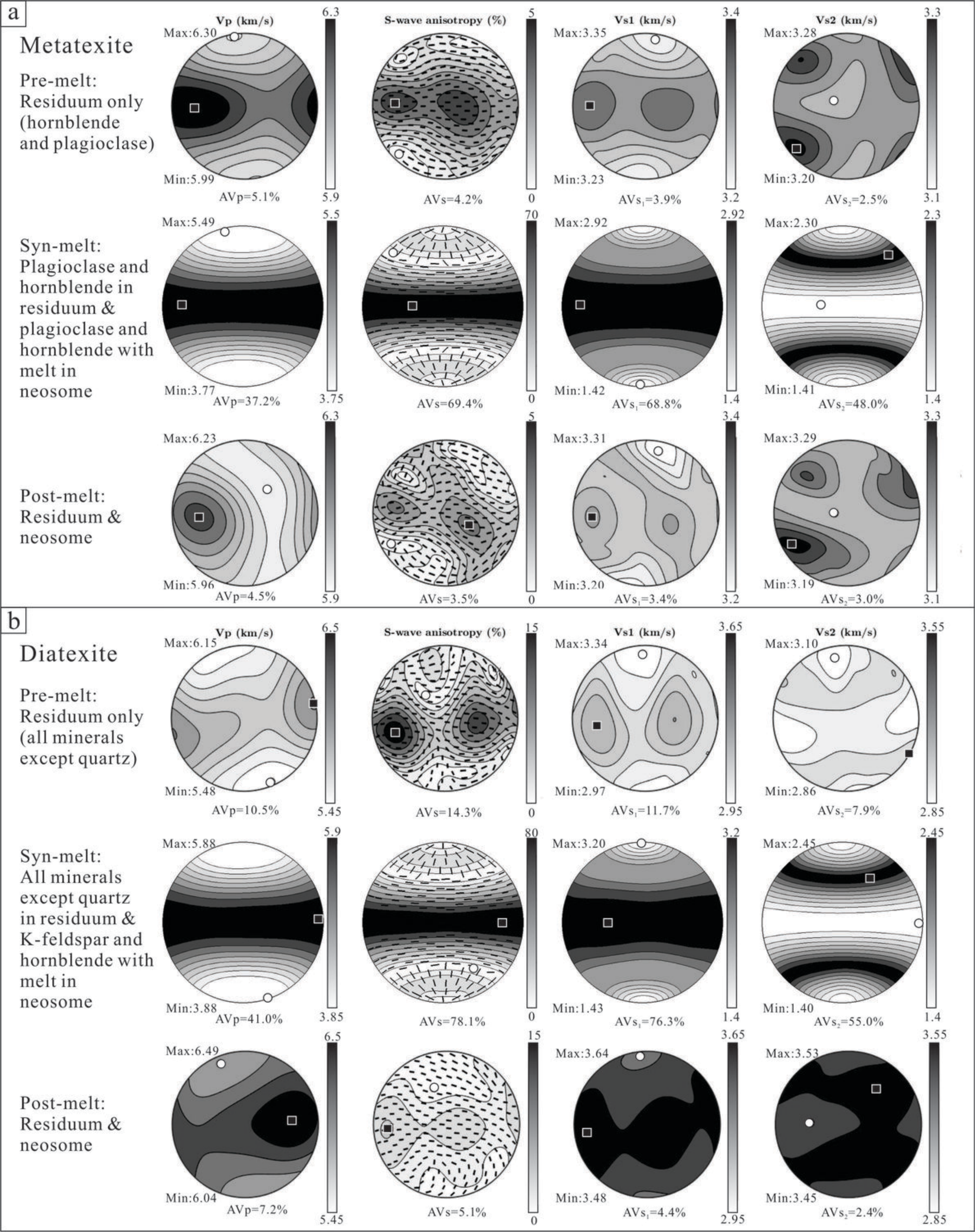

a
Metatexite
Pre-melt: Residuum only (hornblende and plagioclase)
Syn-melt: Plagioclase and hornblende in residuum & plagioclase and hornblende with melt in neosome
Post-melt: Residuum & neosome
Vp (km/s)
S-wave anisotropy (%)
Vs1 (km/s)
Vs2 (km/s)
Max:6.30
Min:5.99
AVp=5.1%
AVs=4.2%
Max:3.35
Min:3.23
AVs1=3.9%
Max:3.28
Min:3.20
AVs2=2.5%
Max:5.49
Min:3.77
AVp=37.2%
AVs=69.4%
Max:2.92
Min:1.42
AVs1=68.8%
Max:2.30
Min:1.41
AVs2=48.0%
Max:6.23
Min:5.96
AVp=4.5%
AVs=3.5%
Max:3.31
Min:3.20
AVs1=3.4%
Max:3.29
Min:3.19
AVs2=3.0%
b
Diatexite
Pre-melt: Residuum only (all minerals except quartz)
Syn-melt: All minerals except quartz in residuum & K-feldspar and hornblende with melt in neosome
Post-melt: Residuum & neosome
Max:6.15
Min:5.48
AVp=10.5%
AVs=14.3%
Max:3.34
Min:2.97
AVs1=11.7%
Max:3.10
Min:2.86
AVs2=7.9%
Max:5.88
Min:3.88
AVp=41.0%
AVs=78.1%
Max:3.20
Min:1.43
AVs1=76.3%
Max:2.45
Min:1.40
AVs2=55.0%
Max:6.49
Min:6.04
AVp=7.2%
AVs=5.1%
Max:3.64
Min:3.48
AVs1=4.4%
Max:3.53
Min:3.45
AVs2=2.4%

Rock type	Condition	Vp_max (km/s)	Vp_min (km/s)	Vs_1_max (km/s)	Vs_1_min (km/s)	Vs_2_max (km/s)	Vs_2_min (km/s)	Max Vp Anisotropy	Max Vs Anisotropy
Metatexite	Pre-melt	6.30	5.99	3.35	3.23	3.28	3.20	5.1	4.2
	Syn-melt	5.49	3.77	2.92	1.42	2.30	1.41	37.2	69.4
	Post-melt	6.23	5.96	3.31	3.20	3.29	3.19	4.5	3.5
Diatexite	Pre-melt	6.15	5.48	3.34	2.97	3.10	2.86	10.5	14.3
	Syn-melt	5.88	3.88	3.20	1.43	2.45	1.40	41.0	78.1
	Post-melt	6.49	6.04	3.64	3.48	3.53	3.45	7.2	5.1

Max Vs_1 Anisotropy	Max Vs_2 Anisotropy	Vp/Vs_1 max	Vp/Vs_1 min	Vp/Vs_2 max	Vp/Vs_2 min
3.9	2.5	1.89	1.83	1.96	1.85
68.8	48.0	2.66	1.68	3.88	1.89
3.4	3.0	1.89	1.80	1.95	1.84
11.7	7.9	1.94	1.74	2.15	1.82
76.3	55.0	2.73	1.62	4.22	1.84
4.4	2.4	1.81	1.72	1.87	1.74